Ab initio study of iron and iron hydride: I. Cohesion, magnetism and electronic structure of cubic Fe and FeH

1998 J. Phys.: Condens. Matter 10 5081

(http://iopscience.iop.org/0953-8984/10/23/012)

J. Phys.: Condens. Matter **10** (1998) 5081–5111. Printed in the UK PII: S0953-8984(98)90967-5

Ab initio study of iron and iron hydride: I. Cohesion, magnetism and electronic structure of cubic Fe and FeH

C Elsässer†‡‖, J Zhu†¶, S G Louie†, M Fähnle‡ and C T Chan§+

† Department of Physics, University of California, Berkeley, CA 94720, USA
‡ Max-Planck-Institut für Metallforschung, Heisenbergstrasse 1, D-70569 Stuttgart, Germany
§ Ames Laboratory and Department of Physics, Iowa State University, Ames, IA 50011, USA

Received 23 January 1998

Abstract. The *ab initio* mixed-basis pseudopotential method based on the density-functional theory is applied to study the cohesion, ferromagnetism and electronic structure of iron and iron monohydride with cubic crystal structures. Spin-unpolarized and spin-polarized calculations are used to assess the transferability of norm-conserving ionic pseudopotentials for iron, and the level of accuracy obtainable for structural equations of state with reasonable effort. The influence of generalized gradient corrections on the cohesive properties is investigated. The results are compared directly to corresponding all-electron results obtained by using both FLAPW and LMTO–ASA methods.

1. Introduction

To give a quantitatively accurate description of the interaction of light particles like hydrogen isotopes, which are distributed over interstitial sites in transition-metal lattices, with the host-metal atoms, the *ab initio* total-energy methods based on the density-functional theory [1] in the local density approximation [2] have been found to be very useful and reliable (see, e.g., chapter 5 in reference [3] or chapter 6 in reference [4]).

Among others things, previous *ab initio* studies concerned with metal–hydrogen systems have given a detailed explanation of the nature of vibrational states of hydrogen isotopes in the 4d transition metals niobium [5, 6] and palladium [7, 8], emphasizing the importance of the anisotropy and the anharmonicity of the corresponding vibrational potentials.

In the present work, which consists of three parts, we systematically continue and extend our *ab initio* study of metal–hydrogen systems to hydrides of 3d transition metals [9], namely body-centred cubic (bcc) α-Fe and Cr, and face-centred cubic (fcc) γ-Fe and Ni. The main focus will be on the Fe–H system for several reasons, detailed below.

There is considerable technological and scientific interest in obtaining an understanding of the interaction of hydrogen with iron because contact with H leads to drastic changes in the mechanical properties of α-Fe, such as serious embrittlement and corrosion of steel, although pure bcc α-Fe under ambient pressure is able to absorb only very small amounts of H in the lattice interstices.

‖ Present address: Max-Planck-Institut für Metallforschung, Seestrasse 92, D-70174 Stuttgart, Germany.
¶ Present address: Lawrence Livermore National Laboratory, Livermore, CA 94551, USA.
+ Present address: Physics Department, Hong Kong University of Science and Technology, Clear Water Bay, Hong Kong.

0953-8984/98/235081+31$19.50

On the other hand, high-pressure experiments motivated recently by geophysical studies of the composition of the Earth's inner core [10] have demonstrated that, under large hydrostatic pressures of several gigapascals, the two-component system of pure iron and pure hydrogen together in a diamond-anvil cell undergoes a structural phase transformation, forming an almost stoichiometric high-concentration iron hydride compound FeH with a close-packed crystal structure of the iron lattice.

In this paper (part I) we investigate the ability of our computational technique, the mixed-basis pseudopotential method [11–14], to describe the structural properties and the electronic structure of bcc and fcc Fe and FeH, including the possibility of a spontaneous spin polarization within the spin-density-functional theory in the local approximation [15] and considering non-local gradient corrections [16–20]. For non-magnetic materials, the success of this method is already well established in the literature. For magnetic materials, however, to our knowledge, there are only few previous pseudopotential studies, dealing with magnetic pure iron. The first one [21], in the early eighties, yielded reasonable but, compared to corresponding all-electron studies, not fully satisfactory results for bcc α-Fe. Recently, nine years later, it has been shown [22] that most of the deficiencies of the early work can be overcome by employing the more powerful computational resources that have become available in the meantime to increase the basis set and thus the accuracy of the results. Further work addressed the accurate description of ferromagnetic iron by pseudopotentials together with a plane-wave basis [23] or a LAPW basis [24]. An *ab initio* molecular dynamics calculation of iron using an orthonormalized-mixed-basis approach is reported in reference [25]. In the present work, besides the extension to iron–hydrogen systems, we carefully re-examine the calculation of structural and magnetic properties of pure iron.

In the second paper (part II [26]) the structural and magnetic properties of close-packed Fe and FeH, namely the hexagonal close-packed (hcp, with a stacking sequence ABAB of close-packed atom planes), double-hcp (dhcp, ABACABAC) and fcc (ABCABC) forms, are discussed and compared to the recent high-pressure experiments [10].

The third paper (part III [27]) is concerned with the discussion of vibrational states and the related adiabatic metal–hydrogen potentials of hydrogen isotopes in two bcc metal hydrides, α-FeH and CrH, and in two fcc metal hydrides, γ-FeH and NiH. These systems illuminate some systematic trends for the characteristic behaviour of vibrational H states when the host metal varies within the transition-metal rows of the periodic table of elements. Furthermore, the influence of magnetism on the vibrational states is discussed. The results of this part form the *ab initio* database used in our recent study of self-trapped states of H isotopes in Fe [28].

2. Computational techniques

In this section, we outline the computational techniques used for the *ab initio* calculations in all three parts of our present work.

2.1. The mixed basis

The present work is based on the mixed-basis pseudopotential method [11–14] (in the following abbreviated as the MBPP method). It combines the merits of *ab initio* pseudopotentials and plane waves, known to be a very successful *ab initio* density-functional method for the calculation of many properties of simple metals, semiconductors and compounds (see, e.g., references [29, 30]), with the ability to describe transition-metal

electron states by including a few localized, atomic-orbital-like functions additionally to the plane waves in a mixed basis set.

For the 3d transition metals and their hydrides, the mixed basis contains approximately 150 plane waves per metal atom, limited by $E_{\mathrm{pw}} = |\boldsymbol{k}+\boldsymbol{G}|^2_{\mathrm{max}} = 24$ Ryd ($\boldsymbol{k}$ is a wavevector in the first Brillouin zone, $\boldsymbol{G}$ is a translation vector of the reciprocal lattice), five local orbitals with d symmetry ($l = 2$) per metal atom, and one local orbital with s symmetry ($l = 0$) per H atom. (The atomic rydberg unit is used for energies; 1 Ryd = 13.606 eV.) A local orbital is constructed from an atomic pseudowavefunction by smoothly cutting off the tail beyond a certain cut-off radius $r_{\mathrm{c}j}$ around the jth atomic site. This cut-off is effected either by multiplying the radial part of the wavefunction with a Gaussian function centred at the cut-off radius and varying the Gaussian width parameter γ_j to minimize the energy (see [13]), or by using a spherical Bessel function $Aj_l(Br)$, whose two parameters A and B are determined by matching the function in value and slope to the atomic pseudowavefunction at $r_{\mathrm{c}j}$, and taking the difference between the wavefunction and the Bessel function for $r \leqslant r_{\mathrm{c}j}$ as the local orbital. The advantage of the second cut-off procedure turns out to be that it does not contain a further parameter to be optimized, and, for the d states, the shapes of the local orbitals obtained in this way are very close to the local orbitals cut off with the Gaussian of optimized width. To allow the crystals' volumes to be changed around the equilibrium value and the position of H in the transition metal to be varied within a sufficiently large portion of the interstitial space to map out the adiabatic vibrational potentials (see part III), the radii $r_{\mathrm{c}j}$ are chosen to be smaller than touching muffin-tin radii, $r_{\mathrm{c,Fe}} = 2.15$ Bohr and $r_{\mathrm{c,H}} = 0.7$ Bohr. (1 Bohr = 0.529 Å is the atomic length unit.) An increase of E_{pw} subsequently up to 48 Ryd shows that the total-energy differences between different crystalline structures (e.g., bcc and fcc) are converged to better than 0.1 mRyd by the mixed basis for $E_{\mathrm{pw}} = 24$ Ryd.

2.2. The total-energy calculations

The structural properties are obtained from differences of density-functional total energies which are calculated employing a momentum-space formalism [31, 32]. The exchange–correlation contribution to the total energy in the local density approximation [2] (LDA) is calculated via a real-space integral. The electron densities needed for total energies are computed in a mixed representation in real and in Fourier space [13], and finally given on a large mesh suitable for fast Fourier transformations (FFT), enclosing plane waves up to wavevectors with lengths less than $|\boldsymbol{G}|^2_{\mathrm{max}}$. The gradients of the electron densities used for the non-local gradient corrections to the exchange–correlation contribution are calculated in Fourier space and obtained in real space via FFT. The accuracy of the Fourier representation of densities, potentials and total energies is monitored by increasing the number of Fourier components successively up to $|\boldsymbol{G}|^2_{\mathrm{max}} = 1600$ Ryd. The total-energy differences are found to be converged to better than 0.1 mRyd for $|\boldsymbol{G}|^2_{\mathrm{max}} = 625$ Ryd.

For the summation of eigenvalues over the first Brillouin zone, equivalent sets of special Chadi–Cohen $\boldsymbol{k}$-points [33, 34] for the different crystal structures and a Gaussian broadening with a width of 0.004 Ryd to mimic the Fermi surface [12, 35] were used. The use of equivalent sets of $\boldsymbol{k}$-points, i.e. the $\boldsymbol{k}$-points for different lattices can be mapped onto each other by symmetry operations, should ensure the best possible cancellation of errors in the discrete summations over the Brillouin zones. For the bcc and fcc structures, in particular, 40 and 60 special $\boldsymbol{k}$-points, respectively, in the irreducible part of the Brillouin zone (corresponding to 20 in the irreducible zone or $8^3 = 512$ $\boldsymbol{k}$-points in the whole Brillouin zone of a simple cubic (sc) Bravais lattice with a 'length cut-off' [34]: $(2l_{\mathrm{cut}}/a_0)^2 = 64$)

were found to give total-energy differences again converged to within 0.1 mRyd for both the spin-unpolarized and spin-polarized cases, as tests with special $\boldsymbol{k}$-points corresponding to those of sc 12^3- and 16^3-meshes confirmed. For the spin-unpolarized bcc and fcc structures even just 8 and 10 irreducible $\boldsymbol{k}$-points ($\simeq 4^3$ sc points), respectively, turned out to be enough to give reasonably accurate results for cohesive properties like the equilibrium volume V_0 and the bulk modulus B_0.

2.3. The ionic pseudopotentials

In pseudopotential theory the influence of the atomic nuclei and the closed-shell core electrons on the valence electrons is described by ionic pseudopotentials. For Fe, and for Cr and Ni discussed in part III as well, we used 'optimally smooth', norm-conserving, non-local pseudopotentials [36] including a non-linear partial-core correction for the exchange–correlation contribution [37]. The atomic reference configuration for the construction of a pseudopotential was chosen according to the occupation numbers of the angular-momentum-decomposed partial charges within an atomic sphere in the elementary metal, which are calculated self-consistently in the LDA using an all-electron LMTO–ASA method (see below; very similar partial charges are obtained for bcc and fcc Fe): $[\mathrm{Ar}]3\mathrm{d}^{\nu+0.6}4\mathrm{s}^{0.6}4\mathrm{p}^{0.8}$ with $\nu = 4$, 6 and 8 for Cr, Fe and Ni, respectively. The comparison of the one-electron eigenstates and excitation energies of the various atomic configurations, as obtained via all-electron and pseudopotential LDA calculation, indicated that this choice of reference configuration yielded a rather good transferability of the pseudopotential for spin-unpolarized LDA and gradient-corrected calculations [9].

The spin-density functional, however, depends very sensitively on the core–valence separation of the non-linear exchange–correlation energy and potential [37]. Therefore a partial-core correction is crucially to be included in the pseudopotential for the treatment of spin-polarized systems. The partial core was cut off at a distance to the nucleus close to the density maximum of the outermost core states, containing essentially the 3s and 3p core states of the 3d transition metals.

The influences of the partial-core correction and the choice of the atomic reference configuration for the construction of a ionic pseudopotential of iron are illustrated in appendix A by means of a comparison of calculated spin-polarization energies and s–d transfer energies for a free iron atom. These results point to a basic problem inherent to the following discussion of structural energy differences between spin-unpolarized and spin-polarized iron crystals: the core–valence separation and the frozen-core approximation, fundamental to the pseudopotential theory, already introduce noticeable deviations of the pseudopotential from the all-electron (i.e. treating the core states explicitly and allowing them to relax as well) results in the energy gain due to spin polarization, which can be as large as a few millirydbergs. Consequently, we have to anticipate that similar deviations may occur as well for structural energy differences between crystals with different lattice structures. Therefore, in parallel with the pseudopotential calculations, we performed all-electron calculations for the structural properties of Fe and FeH to assess the sensitivity of the calculated properties of spin-polarized systems to the approximations in the pseudopotential theory.

For the interaction of the crystal electrons with the H nuclei, the protonic Coulomb potential was used in the present work, part I, to ensure that local magnetic properties like the spin density and the Fermi contact field at H sites are described accurately. As an alternative a local, norm-conserving H pseudopotential [14] was used in the following parts, II and III. For all of the structural and integral magnetic properties, the two potentials lead to the same results.

2.4. All-electron calculations

The two currently very popular standard all-electron methods were used: the full-potential LAPW (FLAPW) method [38–40] and the LMTO method within the atomic sphere approximation (LMTO–ASA) [38, 41].

The FLAPW method is known to describe very accurately structural properties of ideal and distorted crystalline solids. Although there is the basic difference that all electrons are treated explicitly, there are a lot of similarities between the FLAPW and the mixed-basis formalisms, which make the results of the two methods suitable for close comparison. Hence, we tried to choose the calculational FLAPW details as close as possible to the mixed-basis parameters described above: the $\boldsymbol{k}$-point meshes and the Gaussian broadening are the same, the energy cut-off for the augmented plane waves, $E_{\mathrm{apw}} = 20$ Ryd, was chosen slightly smaller only for reasons of practical convenience without reducing the accuracy of the total-energy differences significantly. The augmentation-sphere radius for Fe was 2.15 Bohr. For H, however, a larger radius of 1.05 Bohr had to be chosen to avoid convergence and accuracy problems encountered with a radius of 0.7 Bohr. This detail is of some significance for part III of this work because the larger H radius would limit considerably more the spatial range over which the adiabatic potential of the Fe–H interaction could be mapped out using the FLAPW method with these chosen parameters. For the comparison of the structural, magnetic and electronic properties of FeH, where H is located at stable sites in the lattice interstices, in the present work, part I, the larger H-sphere radius imposes no limitation.

In the LMTO–ASA method, the Wigner–Seitz cells around all atoms in the crystal are replaced by overlapping atomic spheres of the same volumes (avoiding the treatment of space outside touching muffin-tin spheres) and, within each sphere, the electron density and the potential are approximated as being spherically symmetric. Furthermore, a minimal basis of one linear muffin-tin orbital per atomic site and angular momentum component of the valence states is used to represent the one-electron eigenstates. These two approximations drastically reduce the computational effort involved in treating the electron band-structure problem of crystals, and it turns out that the results for the cohesive and magnetic properties for rather densely packed crystal structures like the cubic and hexagonal close-packed and bcc lattices are satisfactorily accurate in many cases, as compared to full-potential results, in spite of the finite overlap of the atomic spheres and the minimal basis. Both latter approximations are improved by using the so-called combined correction in our calculations.

For the calculation of the cohesive properties of pure bcc and fcc Fe presented in this work, part I, the LMTO basis contained s, p, d and f orbitals. For the Brillouin-zone summations, special Monkhorst–Pack $\boldsymbol{k}$-point meshes [34, 42] and the improved tetrahedron method [43] were used instead of special Chadi–Cohen $\boldsymbol{k}$-points and Gaussian broadening (just for computational convenience, not for physical reasons). A subdivision of the unit cells of the reciprocal lattices into 10^3 microparallelepipeds with zero mesh-point displacements was chosen, yielding 47 $\boldsymbol{k}$-points in the cubic irreducible Brillouin zones, which was found to be sufficiently dense for total-energy differences reliable to about 1 mRyd.

2.5. Density-functional approximations

The basic assumption for all practical density-functional calculations lies in the choice of an approximate functional for the exchange–correlation term in the total energy. An extremely successful and thus standard choice is the local density approx-

imation [2] (LDA):

$$E_{\mathrm{xc}}^{\mathrm{LDA}}[\rho_{\mathrm{e}}] = \int_{\Omega} \rho_{\mathrm{e}}(\boldsymbol{r})\epsilon_{\mathrm{xc}}(\rho_{\mathrm{e}}(\boldsymbol{r}))\ \mathrm{d}^3r$$

where $\epsilon_{\mathrm{xc}}(\rho_{\mathrm{e}})$ is taken to be the exchange–correlation energy density of an interacting homogeneous electron gas with the density ρ_{e}.

In the MBPP calculations we apply the parametrization by Perdew and Zunger [44] of the quantum Monte Carlo electron gas data of Ceperley and Alder [45] (denoted by CA in the following). The FLAPW calculations were done using the interpolation formula given by Hedin and Lundqvist [46]. In the LMTO–ASA calculations we used both LDA functionals and found, as shown in the following sections, no significant differences for the results for all structural quantities considered.

The generalization of the LDA for spin-polarized materials is the local spin-density approximation [15] (LSDA):

$$E_{\mathrm{xc}}^{\mathrm{LSDA}}[\rho_{\mathrm{e}}, \rho_{\mathrm{s}}] = \int_{\Omega} \rho_{\mathrm{e}}(\boldsymbol{r})\epsilon_{\mathrm{xc}}(\rho_{\mathrm{e}}(\boldsymbol{r}), \rho_{\mathrm{s}}(\boldsymbol{r}))\ \mathrm{d}^3r$$

where $\epsilon_{\mathrm{xc}}(\rho_{\mathrm{e}}, \rho_{\mathrm{s}})$ is again taken from a spin-polarized interacting homogeneous electron gas with the density $\rho_{\mathrm{e}} = \rho_{\uparrow} + \rho_{\downarrow}$ and the spin density $\rho_{\mathrm{s}} = \rho_{\uparrow} - \rho_{\downarrow}$ ($\rho_{\uparrow}$ and $\rho_{\downarrow}$ are the densities of up- and down-spin electrons). In all our calculations the spin-splitting effect in $\epsilon_{\mathrm{xc}}(\rho_{\mathrm{e}}, \rho_{\mathrm{s}})$ is accounted for by the *ansatz* of von Barth and Hedin [15]. The spin-polarized formulae of Perdew and Zunger [44] and of von Barth and Hedin [15] (the latter, denoted by BH, was used with the slightly modified parameters of Moruzzi *et al* [47]) become the same as the spin-unpolarized ones of Perdew and Zunger and of Hedin and Lundqvist for vanishing spin polarization.

Although the LDA and LSDA have been empirically confirmed to be very successful in the description and prediction of many materials' properties (atoms, molecules and condensed matter), there are several deficiencies remaining which cannot be described satisfactorily in the local approximation. Particular examples are a serious underestimation of the equilibrium volumes of alkali metals [48, 49] and a metallic ground state without an energy gap for some antiferromagnetic transition-metal oxides [50, 51]. One strategy for improving the local approximation, which has been developed and discussed extensively over recent years, is the idea of a generalized gradient approximation (GGA) put forward by Perdew and others, in which the description of the non-local functional E_{xc} is improved by replacing $\epsilon_{\mathrm{xc}}(\rho_{\mathrm{e}})$ by functions which depend on the density and its spatial gradient as well, and which are improvements over the original gradient expansion approximation in that they reproduce several important electron gas properties by construction.

In this work, we used the following gradient-corrected (GC) functionals. The first one is a combination of the GC exchange formula given by Perdew and Wang [18] with the GC correlation formula given by Perdew [16, 17] (in the following called PW, also often denoted as GGA or GGA-I in the literature). In the second one an exchange formula proposed by Becke [19] is combined with Perdew's correlation formula (in the following called BP). The PW functional was used together with all three of our applied band-structure methods, and the BP functional additionally just with the MBPP method.

Recently, Perdew *et al* proposed a new GGA functional [20, 48] (GGA-II or PW91) which, however, is similar to the BP functional. This PW91 formula, in an original implementation by its authors, was available in the WIEN93 FLAPW package [40]. Hence this allowed us to make a direct comparison of the BP and the PW91 results, and to obtain a confirmation of our own previous experience with GC functionals (see appendix C).

3. Cohesive and magnetic properties of Fe

In this section, we compare the cohesive properties of iron in four different crystal states: bcc α-Fe without spin polarization (non-magnetic, bcc NM) and with spin polarization (ferromagnetic, bcc FM), and fcc γ-Fe without spin polarization (fcc NM) and with spin polarization (fcc FM). The results show the long-recognized deficiency of the LDA/LSDA in favouring a close-packed, non-magnetic ground state [52–55], and the subsequent success in resolving this by means of gradient corrections [56–58, 22]. More complicated features such as antiferromagnetic [59–61] and non-collinear [62, 63] spin structures will not be addressed here.

(In the following, for notational convenience, we often omit the separate specification 'LSDA' and denote both cases, spin-unpolarized and spin-polarized calculations in the local approximation, simply by 'LDA', and by 'GC LDA' in the gradient-corrected approximations.)

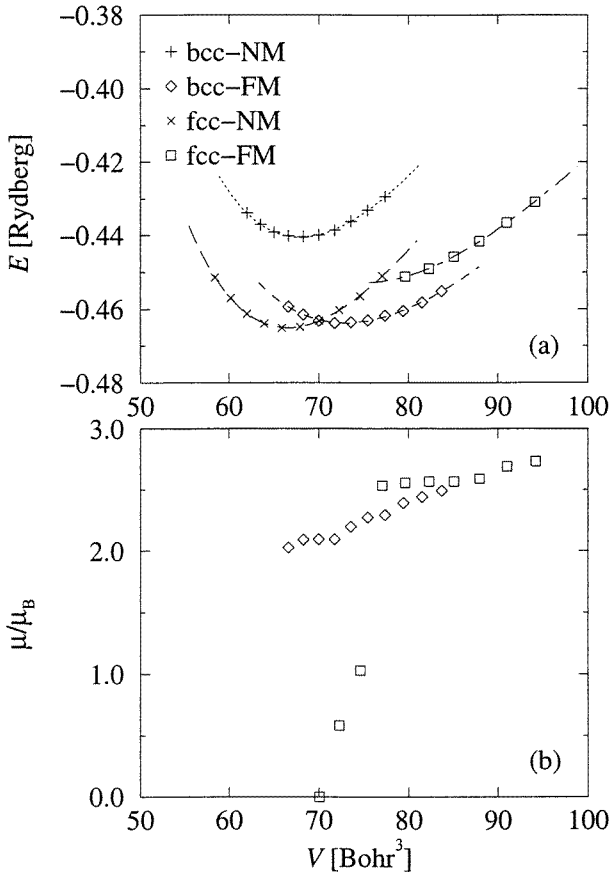

Figure 1. Equations of state of iron crystals calculated in the LDA/LSDA (CA) using the MBPP method. The symbols mark the *ab initio* data points. (a) The energy versus the volume. The lines through the symbols show the fitted EOS of Rose *et al* [64, 65]. (b) The ferromagnetic spin moment versus the volume.

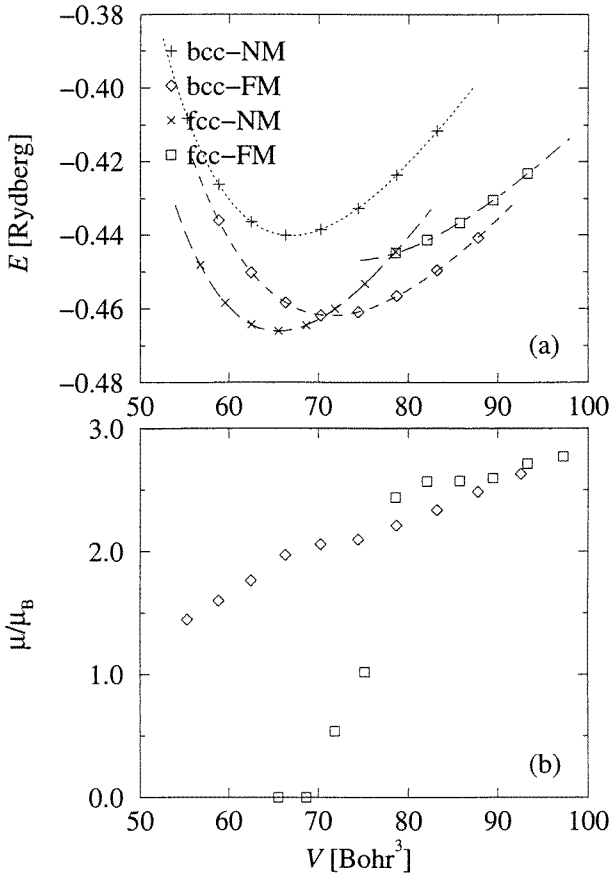

Figure 2. Equations of state of iron crystals calculated in the LDA/LSDA (BH) using the FLAPW method. The symbols mark the *ab initio* data points. (a) The energy versus the volume. The lines through the symbols show the fitted EOS of Rose *et al* [64, 65]. (b) The ferromagnetic spin moment versus the volume.

3.1. Energy–volume curves

The total energies of the crystals versus their unit-cell volumes are displayed in the figures 1(a) to 4(a). Figures 1(a) and 2(a) show the LDA results for $E(V)$ obtained with the MBPP method and the FLAPW method, respectively. Qualitatively they look very similar. However, a quantitative inspection reveals small but noticeable differences. These can be seen more clearly in table 1 where the cohesive parameters V_0, E_0, B_0 and B', as derived by fitting an analytic equation of state (EOS; see appendix B) given by Rose *et al* [64, 65] to the *ab initio* data, are listed.

Our LMTO–ASA, FLAPW and MBPP results can be considered to be in good agreement with each other and, e.g., with the LMTO–ASA results given in [56, 57, 66, 67], the FLAPW results in references [52, 53, 58, 68] and the pseudopotential results in references [22, 23, 24], respectively, under the condition that the desired limit of accuracy for the cohesive parameters is not more strict than a few millirydbergs for the structural energy differences ΔE, a few tenths of Å^3 or eV for V_0 or E_0, respectively, and a few tens of

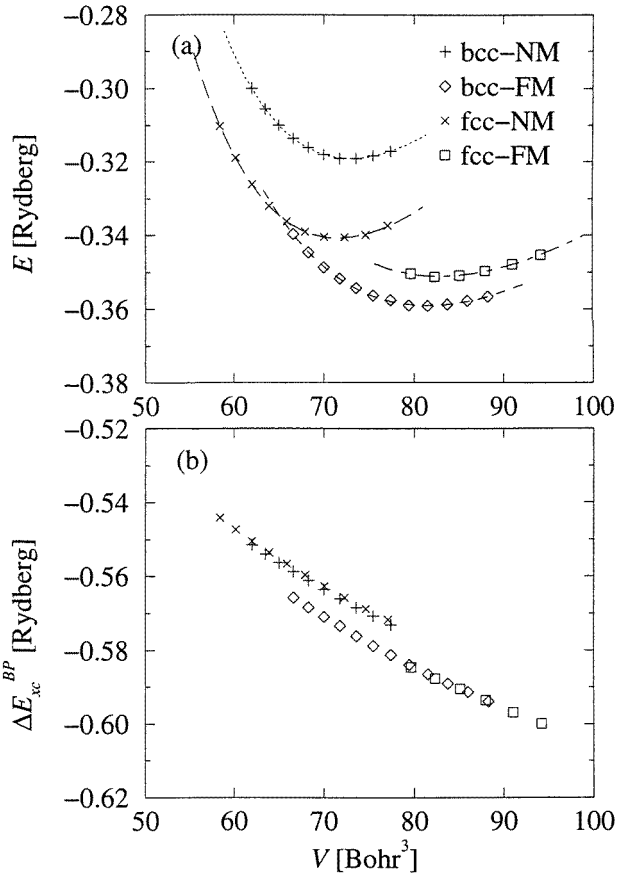

Figure 3. Equations of state of iron crystals calculated with the GC BP functional using the MBPP method. The symbols mark the *ab initio* data points. (a) The energy versus the volume. The lines through the symbols show the fitted EOS of Rose *et al* [64, 65]. (b) The volume dependence of $\Delta E_{\mathrm{xc}}^{\mathrm{BP}}$.

gigapascals for B_0.

Our experience in carrying out the present comparative calculations leads us to predict that achieving a stricter accuracy limit would be onerous, mainly because of the remaining arbitrariness as regards the choice of the number and volume range of the *ab initio* $E(V)$ data used to fit an EOS, and the choice of the model EOS itself, and finally the accurate and unique choice for the free-atom reference energy. These technical variabilities, as discussed in appendix B, allow for changes in the cohesive properties within the limits stated above.

One consequence which we derive from this limitation is that calculations of pressures for structural transitions, which can easily be obtained from any analytic model equation of state, e.g. by common-tangent construction for energy–volume curves or crossing points of enthalpy–pressure curves for two different solid states (where the pressure is given by $p(V) = -\mathrm{d}E/\mathrm{d}V$, and the enthalpy by $H = E + pV$), should be examined cautiously as regards their predictive powers.

For materials containing only one atomic species, such as iron, uncertainties within the limits mentioned above may invoke an uncertainty of several gigapascals in structural

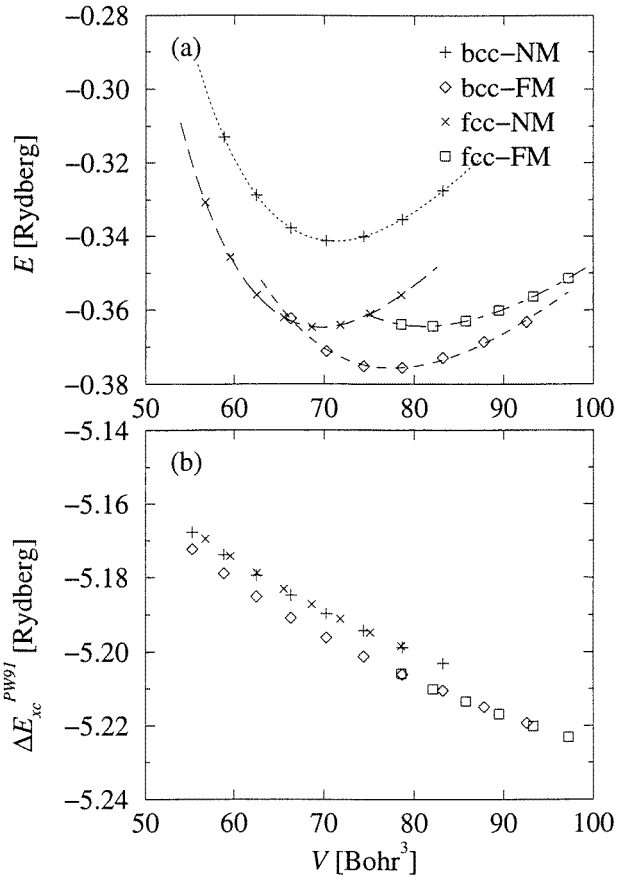

Figure 4. Equations of state of iron crystals calculated with the GC PW91 functional using the FLAPW method. The symbols mark the *ab initio* data points. (a) The energy versus the volume. The lines through the symbols show the fitted EOS of Rose *et al* [64, 65]. (b) The volume dependence of $\Delta E_{\mathrm{xc}}^{\mathrm{PW91}}$.

transition pressures. This can easily be envisaged by means of a simple second-order-polynomial EOS (as was done in a preliminary report of our work [69]).

For materials containing more than one atomic species, such as iron hydride, the uncertainties in the transition pressures, such as in the formation of close-packed FeH from bcc Fe and liquid hydrogen (see part II), are even larger, because here the cohesive energies E_0 of all contributing species, which are (besides their well-known systematic overestimation in the LDA) also rather difficult to obtain with the same and sufficient accuracies, are crucial in the calculation if one is to obtain all of the energies of the different species with respect to a common zero level.

All of these findings discouraged us from trying any more to derive pressures for structural transitions in the Fe and FeH systems, since no method has been found for obtaining cohesive properties and EOS to a higher level of accuracy for transition metals like iron (although there has been success in the cases of simple metals and covalent semiconductors) than is provided by the present state-of-the-art total-energy methods in the LDA or including gradient corrections.

Table 1. The cohesive parameters V_0, E_0, B_0 and B' of non-magnetic (NM) and ferromagnetic (FM) iron with face-centred cubic (fcc) and body-centred cubic (bcc) crystal structure; ΔE is the energy difference with respect to bcc FM Fe; δE is the energy difference of bcc Fe with respect to fcc Fe in the same magnetic state.

		fcc					bcc					
xc functional	Spin polarization	V_0 (Å^3)	E_0 (eV)	B_0 (GPa)	B'	ΔE (mRyd)	V_0 (Å^3)	E_0 (eV)	B_0 (GPa)	B'	ΔE (mRyd)	δE (mRyd)
MBPP												
LDA CA	NM	9.85	6.33	321	4.5	−1	10.06	6.00	314	4.6	23	24
	FM	11.13	6.16	200	4.0	12	10.80	6.31	199	3.9	0	−12
BP	NM	10.59	4.64	255	4.8	18	10.80	4.34	248	4.9	40	22
	FM	12.26	4.78	139	4.0	8	12.07	4.89	150	4.0	0	−8
PW	NM	10.95	4.40	240	4.9	20	11.15	4.12	233	5.0	41	21
	FM	12.69	4.56	141	4.1	8	12.45	4.67	146	4.1	0	−8
FLAPW												
LDA BH	NM	9.70	6.34	343	4.6	−4	9.91	5.98	324	4.7	22	26
	FM	10.89	6.08	197	4.0	15	10.58	6.29	243	4.2	0	−15
PW91	NM	10.31	4.96	283	4.8	11	10.54	4.64	270	4.9	34	23
	FM	12.01	4.96	163	4.1	9	11.49	5.11	180	4.2	0	−11
PW	NM	10.62	4.04	261	5.1	11	10.84	3.74	249	5.2	33	22
	FM	12.33	4.03	165	4.5	12	11.73	4.19	188	4.6	0	−12
LMTO–ASA												
LDA CA	NM	9.74	6.70	347	4.5	−4	9.98	6.36	327	4.6	21	25
	FM	11.11	6.43	214	4.0	16	10.64	6.65	251	4.2	0	−16
LDA BH	NM	9.77	6.67	345	4.6	−3	10.01	6.33	325	4.6	21	24
	FM	11.14	6.41	211	4.0	16	10.67	6.62	250	4.2	0	−16
PW	NM	10.70	4.76	271	4.9	14	10.98	4.46	253	4.9	36	22
	FM	12.52	4.82	166	4.3	9	12.11	4.95	147	4.0	0	−9
Experiment [95, 96]												
	NM	12.06	—	133	—	—	—	—	—	—	—	—
	FM	—	—	—	—	—	11.82	4.28	168	—	—	—

(We are aware of, e.g., the recent *ab initio* PW91 results on structural transition pressures in iron obtained by Stixrude *et al* [68] which are quoted as being in excellent agreement with experiment, but from our own experience discussed above we remain to some extent sceptical as regards the absolute reliability of this positive conclusion.)

In figures 3(a) and 4(a), our $E(V)$ results for Fe obtained with the MBPP method and the BP functional on one hand and with the FLAPW method and the PW91 functional on the other hand are displayed. (As mentioned above, the BP and PW91 functionals are mathematically rather similar and making a direct comparison of results obtained by the two total-energy methods using each one of these functionals is hence as justified as making a comparison using the older PW functional in the two methods, which leads to the same conclusion as the following discussion.)

The effect of the gradient corrections can be understood as a systematic expansion of the equilibrium volume, as compared to that of the LDA $E(V)$ curves in figures 1(a) and 2(a), connected with a crystal-softening decrease in the bulk modulus. The self-consistent total-energy differences between the curves in figures 1(a) and 3(a), and in figures 2(a) and

4(a) are given to a high accuracy by the total-energy contribution $\Delta E_{xc}^{GC}[\rho_e]$ due to the gradient correction. The self-consistent densities ρ_e in the LDA and in the GC LDA turn out to be so similar that in most cases ρ_e^{LDA} can be used to calculate ΔE_{xc}^{GC} with sufficient accuracy, hence saving the additional effort that would otherwise be required to obtain ρ_e^{GC} self-consistently.

The quantity $\Delta E_{xc}^{GC}[\rho_e^{LDA}]$ versus V in the MBPP calculations is plotted in figure 3(b). Figure 4(b) shows the actual self-consistent GC LDA total-energy differences of the FLAPW calculations (with the BH formula in the LDA and with the CG PW91 formula, whose local part is again based on the Ceperley–Alder electron gas data). The slopes and curvatures of the curves in the two figures are remarkably similar over the whole total-energy range plotted. This result demonstrates the ability of the MBPP method to calculate GC total energies for transition metals like iron, provided, however, that the partial core used in the non-linear xc core correction has been chosen judiciously, e.g. in the way discussed in appendix A, to include the outermost core electrons (by means of making the correction PC2 in the present case).

For other partial-core choices, the $\Delta E_{xc}^{GC}(V)$ curves may look very different, for example having a small slope only in the case of no core correction at all, or already a noticeably too steep slope, compared to the FLAPW result, for the correction PC3. Therefore we conclude that the particular choice of PC2, replacing the total-core density by a spherical Bessel function inside the outermost core density maximum, is quite justified and is essential for the success of pseudopotential calculations including gradient corrections. (Practical choices for the cut-off radius, which are equally well suited in the cases that we considered, are between the positions of the outermost core density maximum itself and of the turning point next to it towards the inner core.) An alternative is of course the inclusion of the full-core density for the non-linear xc correction, as proposed recently by Cho and Scheffler [24]. This, however, required the use of a LAPW basis with its angular momentum representation of the strongly varying full-core density within the ionic core region. This is computationally more complicated than a plane-wave basis or, still, the mixed basis together with the momentum-space representation of the partial-core and valence densities, which is usually a very advantageous formulation for pseudopotential calculations.

3.2. Moment–volume curves

The magnetic spin moments per unit cell versus the unit-cell volumes for bcc and fcc iron, obtained in the LSDA with the MBPP method and the FLAPW method, are shown in figures 1(b) and 2(b), respectively. The results obtained by the two methods agree very well. For the bcc crystal the spontaneous spin polarization is stable over the whole volume range around V_0 considered, with an equilibrium value $\mu_s(V_0) = 2.13\ \mu_B$ (μ_B is the Bohr magneton) in close accordance with many previous calculations and with experiment (the total moment $\mu_{exp} = 2.22\ \mu_B$ with dominant spin and 'quenched' orbital contributions of $2.13\ \mu_B$ and $0.09\ \mu_B$, respectively [70]) as well.

(The slightly uneven structure of the $\mu(V)$ data, which does not matter for our present discussion, is an artefact of the sparse IBZ sampling, with only 40 (bcc) and 60 (fcc) special $\boldsymbol{k}$-points and the Gaussian broadening of 0.004 Ryd, and it vanishes for denser $\boldsymbol{k}$-point meshes.)

For the fcc crystal, our calculations yield the well-known breakdown of the magnetic spin moment for volumes smaller than V_0, from a ferromagnetic high-spin (HS) state via a metastable ferromagnetic low-spin (LS) state to the non-magnetic (NM) state. The successful description of this magnetic structure change in γ-Fe, which is quite difficult to

find in unconstrained spin-polarized calculations and can be obtained more easily, e.g., by a fixed-spin-moment technique [59], provides further support for the assertion that the MBPP method, in which the spin magnetism is exclusively due to the valence states, is just as applicable for magnetic systems as the all-electron FLAPW method, in which closed-shell spin-up and spin-down core states are allowed to react independently to the valence spin polarization. This allows us to address the magnetic properties of the Fe–H system below and in parts II and III.

4. Cohesive and magnetic properties of FeH

This section deals with the cohesive properties of the stoichiometric iron monohydrides FeH in which the H atoms occupy a sublattice of interstitial sites with minimal total energy. In γ-FeH these are the octahedral sites of the fcc lattice, like in other fcc transition-metal monohydrides (NiH, PdH; see, e.g., chapter 3 in reference [71]). In α-FeH, like in other bcc transition-metal monohydrides (NbH, TaH; see, e.g., chapter 2 in [71]), the H atoms are located at tetrahedral sites of the bcc lattice.

Table 2. The cohesive parameters V_0, E_0, B_0 and B' of non-magnetic (NM) (or low-spin (LS)) and ferromagnetic (FM) (or high-spin (HS)) iron monohydride with face-centred cubic (fcc) and body-centred cubic (bcc) crystal structure; ΔE is the energy difference with respect to fcc FM/HS FeH.

		NM/LS					FM/HS				
Ab initio method	xc functional	V_0 (Å^3)	E_0 (eV)	B_0 (GPa)	B'	ΔE (mRyd)	V_0 (Å^3)	E_0 (eV)	B_0 (GPa)	B'	ΔE (mRyd)
bcc											
MBPP	LDA CA	12.87	8.47	238	4.0	51	13.71	8.84	189	3.7	24
	BP	13.82	6.50	197	4.2	54	15.02	7.08	150	3.8	11
	PW	14.31	6.18	183	4.3	55	15.52	6.76	143	3.9	41
fcc											
MBPP	LDA CA	11.79	9.12	295	4.1	3	12.44	9.17	216	3.7	0
	BP	12.59	7.01	245	4.3	18	13.68	7.24	176	3.9	0
	PW	12.98	6.68	233	4.4	17	14.05	6.92	176	4.0	0
FLAPW	LDA BH	11.77	8.85	289	4.1	−4	12.32	8.80	200	3.7	0
	PW91	12.45	7.21	255	4.3	6	13.55	7.31	165	3.8	0
	PW	12.84	6.24	235	4.5	7	13.95	6.32	155	3.9	0
LMTO–ASA	LDA CA	11.47	9.28	315	4.1	0	12.03	9.28	213	3.6	0
	LDA BH	11.51	9.08	314	4.2	0	12.10	9.08	216	3.7	0
	PW	12.55	6.81	250	4.4	13	13.64	6.99	175	3.9	0

4.1. Energy–volume curves

In figure 5(a) the volume dependences of the total energies for α-FeH (with H located at tetrahedral interstitial sites) and for γ-FeH (H at octahedral sites), calculated in the LDA by the MBPP method, are displayed. The corresponding cohesive parameters, obtained by

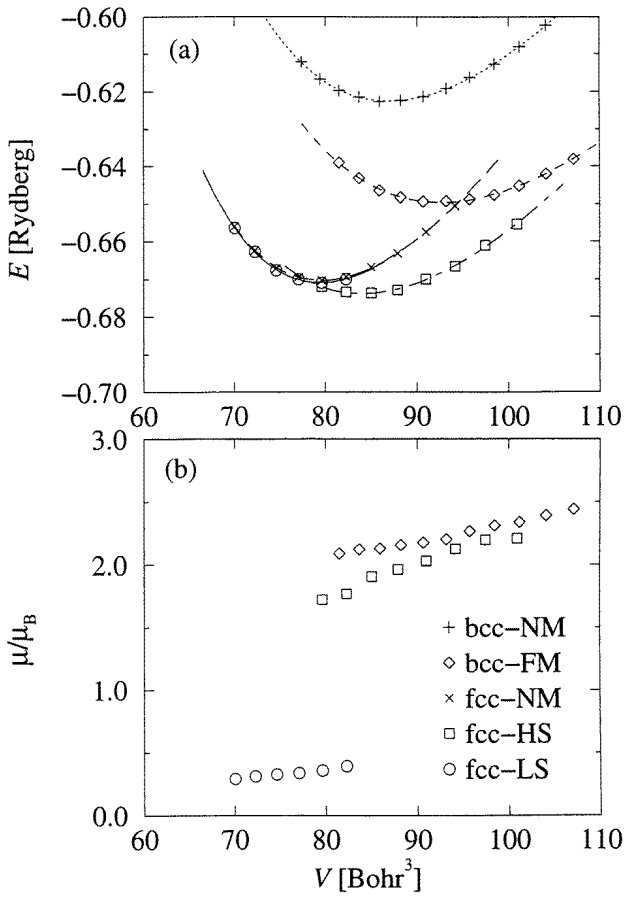

Figure 5. Equations of state of iron monohydride crystals (fcc with octahedral H, bcc with tetrahedral H) calculated in the LDA/LSDA (CA) using the MBPP method. The symbols mark the *ab initio* data points. (a) The energy versus the volume. The lines through the symbols show the fitted EOS of Rose *et al* [64, 65]. (b) The ferromagnetic spin moment versus the volume.

fitting the Rose *et al* EOS [64, 65] to the $E(V)$ data in the LDA and in the GC LDA, are listed in table 2.

Comparing the minimum total energies of the two crystal structures, bcc and fcc, in the three magnetic states, NM, HS and LS, we notice that the previously suggested bcc iron monohydride is theoretically much higher in energy than the fcc FeH, indicating that a close-packed structure should be preferred for the formation of a high-concentration FeH compound (see part II). Hence in the remainder of this section we confine our discussion to γ-FeH.

Like in the previous section, our MBPP results for the cohesive properties of γ-FeH are compared to our corresponding results obtained using the FLAPW and the LMTO–ASA methods, which are also included in table 2.

Energetically, the ferromagnetic LS state of the monohydride is almost indistinguishable from the NM state.

The LDA results for V_0, E_0, B_0 and B' obtained by the MBPP (CA-xc) and FLAPW (BH-xc) methods agree excellently for the NM (LS) state, and still very well for the HS state.

The LDA LMTO–ASA data demonstrate that there is indeed only a marginal difference between using the CA-xc formula and the BH-xc formula.

Looking at the total-energy differences, however, we find that the NM (LS) state turns out to be slightly more stable than the HS state by a few millirydbergs in the FLAPW case, whereas in the MBPP case there is an opposite stabilization of the HS state by about the same amount, and in the LMTO–ASA case the LS and HS states are energetically degenerate.

The corresponding situation arises for pure Fe; that is, for the LDA total-energy difference between fcc NM and bcc FM structures (see table 1), FLAPW and LMTO–ASA results on one hand agreed (4 mRyd in favour of fcc NM structure) and MBPP results on the other hand indicated a slightly different value (1 mRyd, but still in favour of fcc NM structure). Therefore we hesitate to state that the discrepancy for FeH marks a crucial distinction in favour of the accuracy of one of the methods. Instead we tend to conclude that it merely illustrates the limit of accuracy inherent to practical implementations of the different computational representations of the LDA for crystals. A survey of state-of-the-art *ab initio* LDA calculations for pure iron (see, e.g., table 4.1 in [9]) yields values for this energy difference ranging from 8 mRyd in favour of fcc NM structure [72] to even 2 mRyd in favour of bcc NM structure [73], depending on the details of the various LDA band-structure techniques. Of course, in the limit of a 'pure' LDA/LSDA, independent of any basis-set representation or xc interpolation formula, there should be definitive values for structural total-energy differences, but at the level of refinement obtained in our study (see section 2) we are confident in stating that fcc NM and bcc FM states for pure Fe or fcc NM (LS) and fcc HS states for FeH are almost degenerate in the LDA.

Upon using gradient corrections for FeH, the fcc HS state definitely becomes stabilized with respect to the fcc LS state according to all three methods, however again with noticeably different energy gains (for the PW functional, 11 mRyd with the FLAPW method, 17 mRyd with the MBPP method and 13 mRyd with the LMTO–ASA method). The other cohesive properties of FeH are modified by the gradient corrections in the same systematic fashion as was already found for pure Fe in the previous section: V_0 and B' are increased, and B_0 and E_0 are reduced, very similarly for the BP and PW91 functionals and more strongly for the PW functional.

4.2. Moment–volume curves

The volume dependences of the ferromagnetic spin moments per unit cell for the iron monohydrides are shown in figure 5(b). The moment for bcc FM FeH, like that for bcc FM Fe, is stable over the whole volume range around V_0 considered, with a value of similar magnitude to but slightly larger than 2 μ_B and a slow increase with the volume.

For fcc FeH, the ferromagnetic HS state has noticeably smaller values for the spin moments than for pure Fe; this is because of the interaction with the interstitial H atoms. The instability of the HS state upon compression of the volume appears at about the same crystal volume as in the case of fcc Fe, but this state changes to a different LS state with a small but finite spin moment of about 0.3 μ_B. This result obtained with the MBPP method is also found with the FLAPW method; they are in perfect agreement with each other. (With the LMTO–ASA method, however, we have not succeeded in finding this LS state in the unrestricted LSDA calculations. If it is not suppressed by the spherical approximation, it might be found using the fixed-spin-moment technique.)

Summarizing this and the previous sections on the cohesive and magnetic properties of cubic Fe and FeH, we have demonstrated that these quantities can be described similarly

well using pseudopotentials and a mixed basis or all-electron augmented-basis methods with or without shape approximations for the crystal potentials. In particular, for quantities like some of the structural total-energy differences (of few millirydbergs) discussed above, we hope to have shown by comparison of the results obtained with three methods that none of these methods seems to be obviously superior to the others. This encourages us to confine our following presentation to results obtained with the MBPP method and, in part II only, to results obtained from the more computer resource saving (and, for $E(V)$ and $\mu(V)$ studies, in most cases sufficiently accurate) LMTO–ASA method.

5. Electronic structures of Fe and FeH

In this section, results of spin-polarized mixed-basis pseudopotential calculations for the electronic structures of the valence electrons in Fe and in FeH are presented.

In a recent work, Papaconstantopoulos [74] investigated all transition-metal monohydrides with NaCl structure (i.e., with a fcc lattice of the metal atoms and occupation of all octahedral interstitial sites of the fcc lattice with H atoms) for their possibilities of exhibiting a ferromagnetic order, by means of LDA total-energy and band-structure calculations without spin polarization using the Stoner criterion [75–77]. Of the thirty metal hydrides considered, CoH was the only one exceeding the Stoner limit for magnetic instability, while RhH and FeH just failed to reach it by a small amount. In subsequent calculations for CoH, including spin polarization, Singh and Papaconstantopoulos [78] found a stable ferromagnetic state with a magnetic spin moment of $\mu_s = 1.16\ \mu_B$ per formula unit, which is smaller than the spin moment of pure Co ($\mu_s = 1.62\ \mu_B$) because of the additional valence electron. However, because of the strong attraction of the interstitial H potential, it is still considerably larger than the spin moment of isoelectronic Ni ($\mu_s = 0.59\ \mu_B$).

Our spin-polarized calculations yield stable states with ferromagnetic order also for FeH, whose cohesive properties have been described in the previous section. The electronic structures of fcc FM γ-Fe and γ-FeH are compared with the results for CoH. Then the electronic structures of bcc FM α-Fe and of hypothetical α-FeH are presented.

5.1. H in fcc γ-Fe

Fe and FeH with close-packed crystal structures (hcp, dhcp and fcc) are characterized by very similar cohesive properties. This will be demonstrated in part II. The same observation holds for their electronic structures, assuming these to be represented by their total densities of states (DOS). Therefore, in this section, only the DOS for fcc FM Fe and FeH, as examples representative of the other close-packed structures, are discussed. All the DOS were calculated for the equilibrium unit-cell volume in the LSDA.

Figure 6(a) shows the DOS of pure fcc FM γ-Fe, a strong ferromagnet like fcc Co, with completely filled majority d bands but only about half-filled minority d bands.

The major changes in the DOS on the formation of the monohydride FeH are illustrated in figures 6(b) and 6(c). The additional electron per unit cell contributed by the H atom causes an upward shift of the Fermi level, increasing the filling of the majority sp bands slightly and the filling of the minority d bands more strongly. This results in a reduction of the band splitting, visible as the relative energy shifts of the highest peaks originating from d states in the spin-up and spin-down DOS, respectively, and a reduction of the total magnetic spin moment. The strong attractive electrostatic potential of the interstitial proton causes a splitting off of the lowest band filled with two electrons, whose charge density is accumulated and almost spherically distributed around the proton (cf. figure 8 below).

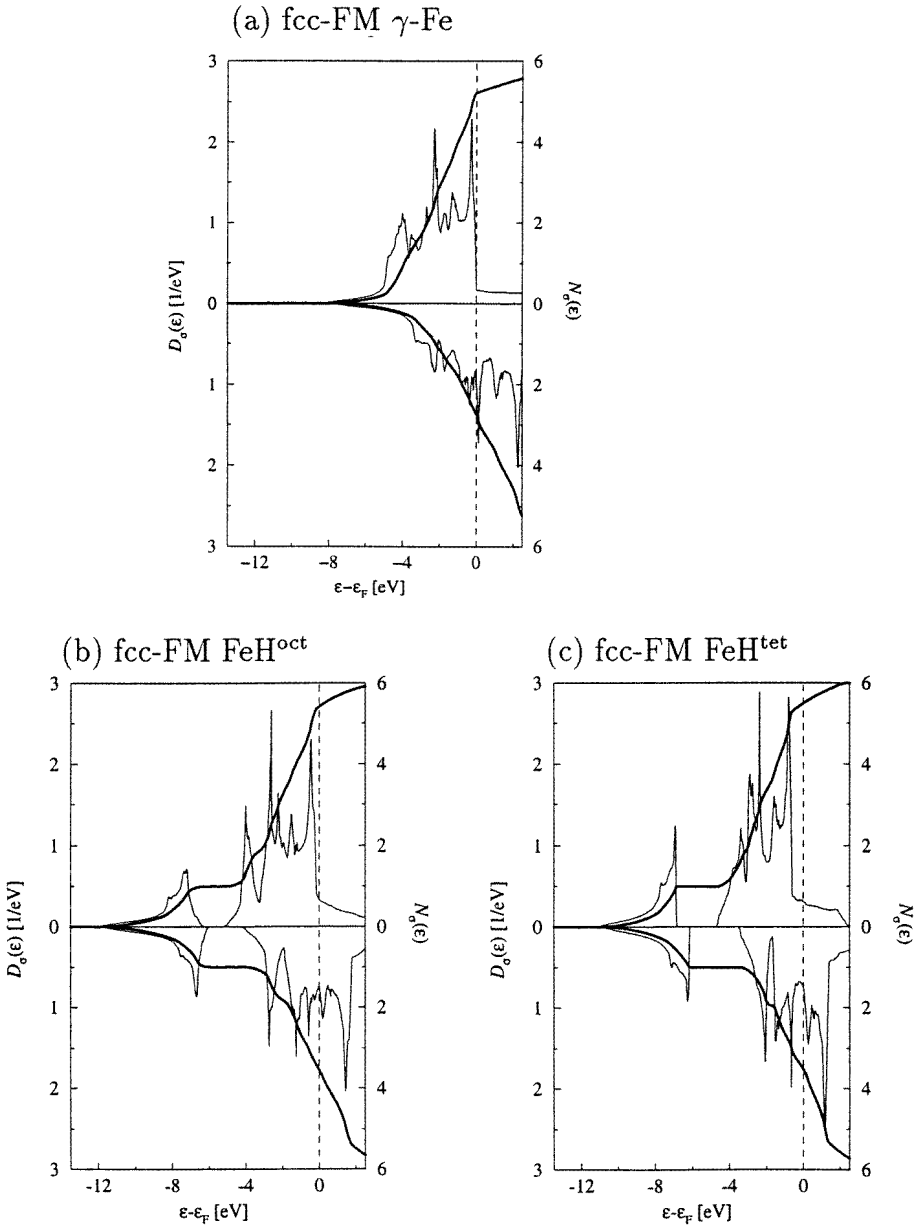

Figure 6. Spin-polarized densities of states of ferromagnetic fcc Fe and FeH (upper parts of the graphs: $\sigma = \uparrow$; lower parts: $\sigma = \downarrow$): (a) fcc FM Fe; (b) fcc HS FeH with octahedral H (NaCl structure); (c) fcc HS FeH with tetrahedral H (ZnS structure).

Both the shift of the Fermi level and the separated lowest band are characteristic changes for hydride formation for fcc metals, and have been studied, as reported in the literature, for many non-magnetic fcc transition-metal hydrides, in particular PdH (cf. chapter 6 of [4] or [9]). Qualitatively, they can be understood by considering first the necessity to accommodate one additional electron in the Fermi sea of the metal, and second a charge

transfer from the metal atoms to the more electronegative H atoms.

The reduction of the magnetic spin moment can be explained for the strong ferromagnet by the fact that all of the majority d states are already full, and that there are more minority d states than majority sp states just above the Fermi level available to be filled with the additional electron. Quantitatively the total magnetic spin moments per unit cell (each at the LSDA equilibrium volume) are reduced from $\mu_s^{\text{pure}} = 2.47\ \mu_B$ for pure γ-Fe to $\mu_s^{\text{oct}} = 1.85\ \mu_B$ and $\mu_s^{\text{tet}} = 1.93\ \mu_B$ for FeH with octahedral- and tetrahedral-site H occupancy, respectively.

5.2. H in bcc α-Fe

As mentioned above, there is no experimental evidence for the formation of stable stoichiometric bcc monohydride FeH. However, a theoretical inspection of the electronic structure of such a hypothetical compound, which has been carried out recently for the construction of an adiabatic-potential model for quantum states of dilute H isotopes in α-Fe [28], is quite instructive qualitatively, for the sake of comparison both with close-packed FeH treated above and with non-magnetic bcc transition-metal hydrides like NbH, which has been thoroughly discussed in the literature (cf. reference [79] or reference [9]).

The DOS of pure bcc FM α-Fe, obtained by the MBPP method in the LSDA, is plotted in figure 7(a), and it is in good agreement with literature results calculated by all-electron methods. A remarkable difference from the DOS of pure fcc γ-Fe, shown in figure 6(a), is that the Fermi level of α-Fe is located within both the majority and minority d bands, characterizing α-Fe as a weak ferromagnet.

The presence of one hydrogen in each one of the tetrahedral and octahedral sites per Fe atom in the bcc lattice leads to the DOS of the hypothetical monohydrides shown in figures 7(b) and 7(c). The most obvious qualitative changes from the DOS of pure α-Fe, i.e., the splitting off of the lowest bands towards lower energies below the d bands and the upward shift of the Fermi level, are similar to those already described for γ-FeH. The latter change makes α-FeH a strong ferromagnet again.

Quantitatively, however, there is almost no change of the majority–minority band splitting, seen as from the relative positions of the highest peaks in the spin-up and spin-down DOS, and the total magnetic moments per unit cell (again with the LDA equilibrium volume), $\mu_s^{\text{tet}} = 2.17\ \mu_B$ and $\mu_s^{\text{oct}} = 2.20\ \mu_B$ for tetrahedral- and octahedral-site H occupancy, respectively, are even slightly increased over that of pure α-Fe, $\mu_s^{\text{pure}} = 2.13\ \mu_B$.

An empirical criterion in the electron theory of metallic materials states that a compound is likely to be stabilized if the Fermi level passes through a valley of the DOS, i.e. it lies in an energy range with a small DOS value. Inspecting figures 7(a)–7(c) and assuming that the partly filled minority d bands are more relevant for the structural stability than the majority d bands, which are almost or completely filled, we notice that for the stable pure α-Fe the Fermi level does indeed lie in a narrow valley in the middle of the minority DOS, whereas for the two FeH compounds it is shifted towards a high peak of the DOS above the valley. This can be considered as an indication of the instability of the bcc FeH compounds, but not necessarily a proof, because the band-energy term

$$\int_{-\infty}^{\varepsilon_F} D(\varepsilon)\varepsilon \, \mathrm{d}\varepsilon$$

in the total energy is only one of several terms governing the structural energies.

In figures 6(a)–6(c) we see that both for pure γ-Fe and for close-packed FeH, which can both be stabilized experimentally at high temperatures or pressures, the Fermi level does

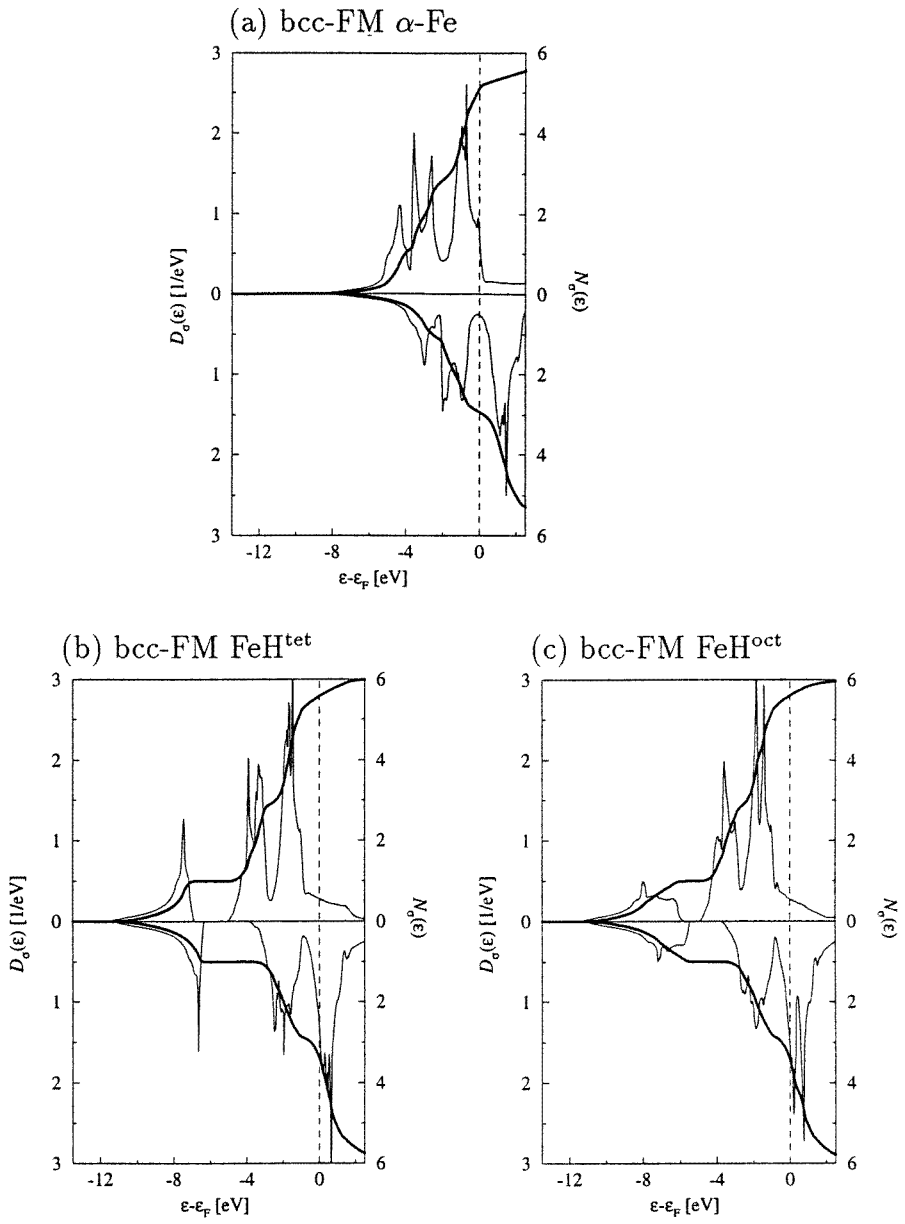

Figure 7. Spin-polarized densities of states of ferromagnetic bcc Fe and FeH (upper parts of the graphs: $\sigma = \uparrow$; lower parts: $\sigma = \downarrow$): (a) bcc FM Fe; (b) bcc FM FeH with tetrahedral H (space group D^{9}_{2d}); (c) bcc FM FeH with octahedral H (space group D^{17}_{4h}).

indeed pass through local minima of the minority DOS. For FeH with tetrahedral-site H occupancy, the Fermi level is slightly shifted away from a local DOS minimum. This can be taken, in accordance with the criterion above, as an indicator that tetrahedral-site-occupied FeH is less stable than the actually observed (and predicted by the *ab initio* calculations; see part III) octahedral-site-occupied FeH. However, we are cautious not to overemphasize

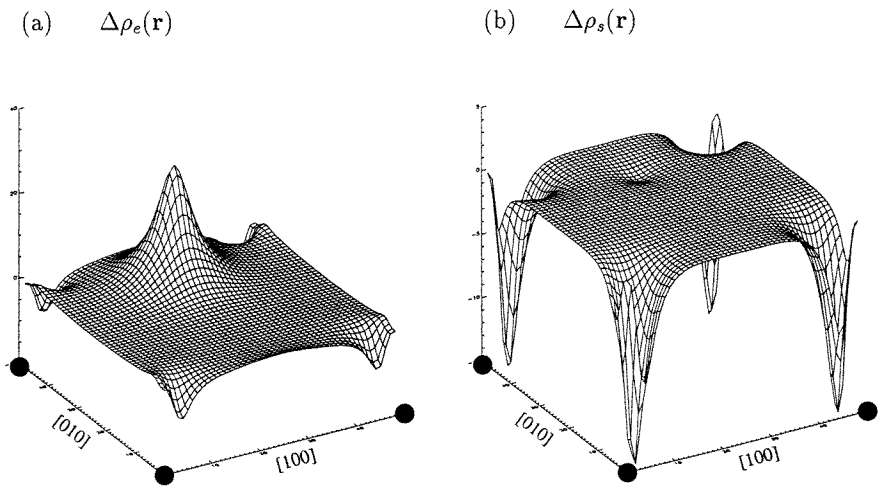

Figure 8. Cuts through (a) the electron-density difference $\Delta\rho_e(\boldsymbol{r})$ and (b) the spin-density difference $\Delta\rho_s(\boldsymbol{r})$ of FeH and Fe in an (001) plane of the bcc crystal lattice. Positions of Fe atoms at the corners are marked by black circles; the tetrahedral H position is below the electron-density maximum in (a) or the spin-density dip in (b). The densities are in arbitrary units.

the predictability of such a subtle effect of the DOS for the structural stabilities of the iron monohydrides. For instance, the influence of lattice vibrations, which are not considered in our study, on structural stability is very important at high pressures and temperatures.

Another way of illustrating the electronic structure of iron and its change caused by the monohydride formation is to look at the real-space electron and spin densities. In the following we focus on two-dimensional cuts through the three-dimensional densities of bcc α-Fe and α-FeH with tetrahedral-site H occupancy in an (001) plane of the cubic lattice passing through Fe atoms.

Figure 8(a) shows such an (001) cut through the electron density ($\rho_e = \rho_\uparrow + \rho_\downarrow$) of α-FeH at its LSDA equilibrium volume, from which the electron density of pure α-Fe at the same volume has been subtracted:

$$\Delta\rho_e = \rho_e(\mathrm{FeH}) - \rho_e(\mathrm{Fe}).$$

This difference in electron density illustrates the distribution of the additional electron from the H atom and the related redistribution of the eight Fe electrons in the unit cell. The position of the H nucleus on a tetrahedral site is located below the electron-density maximum. If no redistribution of the other electrons was caused by the implantation of the H atom, almost zero density differences should appear at the Fe positions (at the four corners of the plot), and the electron-density hill centred at the H position should decay exponentially and contain one electron in total. However, H has a higher electronegativity than Fe and thus additional electron density is transferred from Fe to H. This transfer is manifested in figure 8(a) by the negative sign of $\Delta\rho_e$ around the Fe positions. The aspherical shape of $\Delta\rho_e$ around Fe and its spherical shape around H qualitatively indicate the transfer of electrons from Fe d to H s states, connected with a strong s–d hybridization in the band structure.

The influence of H on the magnetism of Fe can be seen in figure 8(b) where an (001) cut through the spin-density ($\rho_s = \rho_\uparrow - \rho_\downarrow$) difference of α-FeH and of α-Fe (both again

at the same volume, the LSDA equilibrium value of α-FeH) is plotted:

$$\Delta\rho_s = \rho_s(\mathrm{FeH}) - \rho_s(\mathrm{Fe}).$$

At this theoretical equilibrium volume of FeH, the magnetic moments of FeH and of pure Fe are $\mu_s^{tet} = 2.17\ \mu_B$ and $\mu_s^{pure} = 2.64\ \mu_B$, respectively. This means that the strong moment increase of pure Fe from $\mu_s^{pure} = 2.13\ \mu_B$ (at its own theoretical equilibrium volume; see above) caused by the lattice expansion due to H is almost compensated again by the electron- and spin-density redistributions which tend to reduce the local Fe spin moment. This can be identified again from the negative sign of $\Delta\rho_s$ around the Fe positions.

The little dip in $\Delta\rho_s$ centred at the H position indicates the existence of a small magnetic spin moment, which is located at the H atom and has an orientation antiparallel to the large Fe spin moment. (The spin structure of FeH can be envisaged as a ferrimagnetic arrangement with a dominant Fe-sublattice polarization and a very tiny H-sublattice polarization.) This local spin polarization $\rho_s(\mathrm{H})$ can be related to a Fermi contact field B_{Fermi} of the magnetic hyperfine interaction at the H-nucleus site, which in its simplest non-relativistic approximation is proportional to $\rho_s(\mathrm{H})$:

$$B_{\mathrm{Fermi}} = -\frac{2}{3}\mu_0\mu_B\rho_s(\mathrm{H})$$

(in SI units, $\mu_0 = 4\pi \times 10^{-7}$ V s A^{-1} m^{-1} is the magnetic permeability constant, $\mu_B = 9.274 \times 10^{-24}$ A m^{-2} is the Bohr magneton; the unit of ρ_s is m^{-3}).

This quantity is susceptible to investigation in experiments (cf., e.g., [80]) and has been measured quite accurately, e.g. by the muon-spin-rotation technique. Considering the positive muon, μ^+, as a light H isotope and neglecting its spatial delocalization, a measured value of $B_{\mathrm{Fermi}} = -1.06 \pm 0.01$ T [81] can be compared to calculated values discussed in the following.

Akai *et al* [82, 83] calculated B_{Fermi} for one single H atom located at a tetrahedral site in an infinitely extended Fe crystal using a LSDA Green-function technique. Their result of -1.03 T agrees perfectly with the experimental one. Using a LSDA cluster method, Ellis and Lindgren [84] found a value of -1.44 T, noticeably larger than the experimental one, for one tetrahedral H atom in the middle of a free Fe cluster of finite size.

In order to determine B_{Fermi} by the MBPP method we use the protonic Coulomb potential instead of a pseudopotential for H, which is appropriate for a correct description of the local spin density at the H site. In contrast to the case for the two quoted calculations, B_{Fermi} is calculated for H in the monohydride FeH. For the different crystal structures (bcc and fcc) and interstitial H sites (octahedral and tetrahedral), we find similar values of B_{Fermi} at all H sites:

$$B_{\mathrm{Fermi}} = -0.5 \pm 0.1\ \mathrm{T}.$$

This value is considerably lower than the experimental one.

To see whether this discrepancy is related to inadequacies of the pseudopotential technique or the mixed basis, we performed the same calculations for fcc FeH using both all-electron methods again. The FLAPW calculations yield a value of -0.4 T and this confirms nicely the accuracy of the MBPP results. The LMTO–ASA calculations, however, yield -1.0 T, which is in accordance with the finding of Akai *et al* [82, 83].

One possibility for explaining this discrepancy between the results for B_{Fermi} obtained by the different methods might be that the muffin-tin potential approximation underlying the calculations made by Akai *et al* is similar to the ASA in the LMTO method, both leading to higher theoretical values than the FLAPW and MBPP methods, in which no shape approximations are made for the interstitial region around the H site.

Thus the discrepancy between the 'full-potential' results and experimental results may be attributed partly to the fact that the calculation was done for the monohydride with rather closely neighbouring H atoms, whereas the experiment probes B_{Fermi} for essentially one single muon in a macroscopic iron crystal. To prove or disprove this proposal for the explanation, either a large-supercell calculation to model a low H concentration or a full-potential extension of the Green-function work of Akai *et al* is needed.

Concluding this final discussion, however, one has to bear in mind that both the value of about one tesla and the discrepancy of about half a tesla are rather small absolute values for B_{Fermi} (cf. reference [85]). Comparing experimental and theoretical values for heavier interstitial particles in Fe [83], one sees that the absolute differences are typically several teslas for absolute values of several tens of teslas. Therefore the discrepancy of half a tesla between the full-potential or pseudopotential FeH results and the experimental μSR result for the particular case of H in Fe should perhaps not be overemphasized.

6. Summary

In this work we applied the *ab initio* mixed-basis pseudopotential (MBPP) method to a study of the cohesion, magnetism and electronic structure of iron and iron monohydride with cubic crystal structures. The results of spin-unpolarized and of spin-polarized calculations were thoroughly checked as regards the transferability of norm-conserving ionic pseudopotentials for the 3d transition metal Fe for spin-polarized cases and the level of accuracy obtainable with a reasonably large but finite mixed-basis representation of the electron states and densities.

The application of gradient corrections to the LDA/LSDA in a pseudopotential method for transition metals and their influence on the cohesive properties of Fe and FeH were discussed.

Our MBPP results were compared directly with our corresponding all-electron results obtained using both the FLAPW and the LMTO–ASA methods, indicating some limitations of the pseudopotential scheme, in particular in connection with gradient corrections, but a very good overall accordance within the LDA/LSDA. This demonstrates that the MBPP method is computationally competitive with and comparably accurate to the FLAPW all-electron method for both non-magnetic transition metals, which is well documented in the literature, as well as for 3d magnetic transition metals like the 'worst case', magnetic iron.

Acknowledgments

The present work was initiated during a research year for CE at the UC Berkeley. CE gratefully acknowledges the financial support of the Max-Planck Society and the hospitality at Berkeley. This work was supported in part by the National Science Foundation (UC Berkeley: Grant No DMR-9520554) and the US Department of Energy (UC Berkeley: Contract No DE-AC03-76SF00098; Ames Laboratory: Contract No W-7405-ENG-82), including computer time at the NERSC in Livermore and the NCSA in Urbana–Champaign. CE, CTC and MF are grateful for the financial support of the NATO collaborative research grant No 910439. The authors appreciated many valuable discussions with K-M Ho on the mixed basis, pseudopotentials and metal–hydrogen systems, and with A García on generalized gradient corrections.

Appendix A. The free iron atom

In this appendix, the transferability of norm-conserving ionic pseudopotentials for iron, which are constructed from spin-unpolarized atomic valence-electron states, to a spin-polarized case is investigated with respect to its sensitivity to the atomic configuration chosen for the construction (the atomic reference configuration), to the non-linear core–valence xc interaction (i.e. via the partial-core correction) [37] and to generalized gradient corrections.

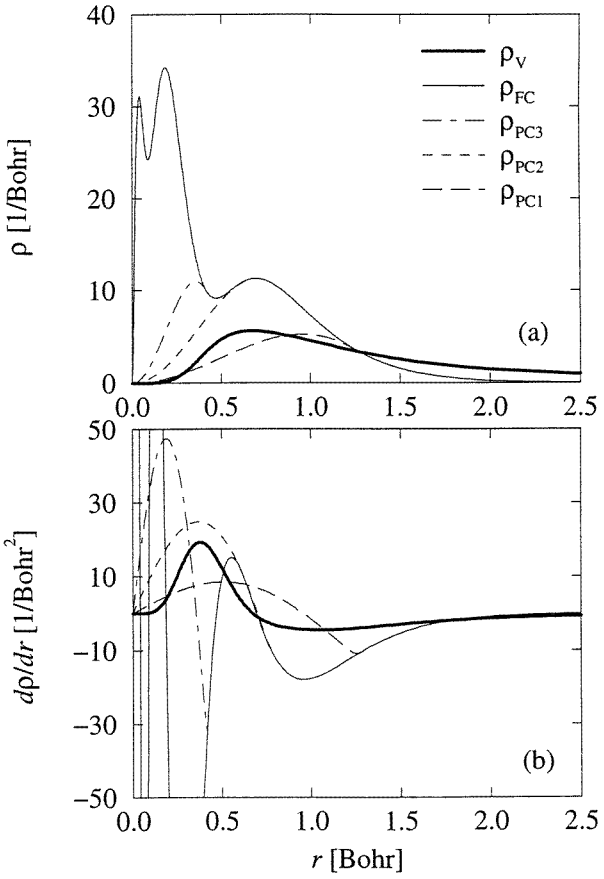

Figure A1. (a) Radial atomic densities and (b) their first derivatives for a free Fe atom in the LDA. The atomic configuration is $[Ar]3d^{6.6}4s^{0.6}4p^{0.8}$. Pseudodensity ρ_v of the valence electrons: thick solid line; frozen density ρ_{FC} of the full core: thin solid line; line styles for partial-core densities: ρ_{PC1}: long-dashed; ρ_{PC2}: short-dashed; ρ_{PC3}: chain.

As mentioned in section 2, the atomic reference configuration for iron was chosen following LMTO–ASA results: $[Ar]3d^{6.6}4s^{0.6}4p^{0.8}$. Figure A1(a) shows the radial core- and valence-electron densities for this configuration, together with three different choices of partial-core densities for the non-linear partial-core correction. The latter are constructed by replacing the full-core density by a spherical Bessel function inside a radius at which the core–valence density ratio ρ_c/ρ_v reaches a given value (PC1, PC2 and PC3 denote the partial cores cut off at $\rho_c/\rho_v = 1$, 2 and 3, respectively).

A first glance to figure A1 might suggest that it may be hopeless to try to get any reasonable result with a pseudopotential calculation because of the huge core–valence density overlap entering the non-linear xc energy density via $\epsilon_{xc}(\rho_c + \rho_v)$ if not even the full frozen-core density is taken into account. This, however, is only easy in a pseudopotential calculation for a free atom, but not in a crystal if momentum-space techniques [31] are to be used.

Fortunately, the following results demonstrate that the situation is less serious. One needs to satisfy only the less stringent requirement that the valence density may not change strongly due to a different chemical environment in that core–valence overlap region, in which the full- and the partial-core densities are markedly different. From this argument, we expect that the partial cores PC2 and PC3 which contain almost the whole outermost core-electron shells (3s and 3p states) should work similarly well to the full core (FC). This will be checked in the following.

Table A1. The influence of the partial-core correction in the non-linear ionic pseudopotential on the energies of a transition $[Ar]3d^64s^2 \rightarrow [Ar]3d^74s^1$ in a spin-unpolarized or spin-polarized free iron atom (energies in millirydbergs; for the meaning of * and the notation in the first column, see the main text).

	Spin-unpolarized			Spin-polarized		
	LDA	BP	PW	LDA	BP	PW
AE	83	78	67	−10	−16	−27
FC	88	83	72	−11	−17	−29
PC3	88	83	72	−11	−18	−36*
PC2	88	83	72	−16	−19	−30
PC1	88	83	72	−62	−64	−77
NC	88	82	72	−161	−162	−163

The influence of the core correction on the total-energy change caused by an electron transition, $[Ar]3d^64s^2 \longrightarrow [Ar]3d^74s^1$ (s–d promotion energy), is given in table A1. (Please note that a FC pseudopotential calculation is not exactly equivalent to an all-electron (AE) calculation because, instead of an AE valence density, the valence pseudodensity is used together with an AE core density. Also, no relaxation or spin polarization of the core is possible, because the frozen spin-unpolarized core of the atomic reference configuration is retained in other chemical environments.)

First, the positive signs for the spin-unpolarized LDA results indicate that the configuration $[Ar]d^6s^2$ is predicted to have a lower energy than $[Ar]d^7s^1$, in contrast to reality and to the LSDA results (negative signs).

Second, we note that, for the spin-unpolarized case, the results are very insensitive to the core correction. Thus, for spin-unpolarized calculations for iron, the core correction is not important and a linear pseudopotential, i.e. one without core correction (denoted by NC for no core in the following), works equally well.

Third, for the spin-polarized case, however, the core correction is essential, and the NC and PC1 results deviate substantially from the FC ones, whereas the PC2 and PC3 results become reasonable.

The same conclusions can be drawn from the data in table A2 where spin-polarization energies, i.e. the energy differences between the non-polarized and spin-polarized calculated results for the same atomic states, for the two lowest states are listed. All of the findings up to now hold equally well for LDA and GC calculations.

Table A2. The influence of the partial-core correction in the non-linear ionic pseudopotential on the spin-polarization energies for two configurations, $[Ar]3d^74s^1$ and $[Ar]3d^64s^2$, of a free iron atom (energies in millirydbergs; for the meaning of * and the notation in the first column, see the main text).

	$[Ar]3d^74s^1$			$[Ar]3d^64s^2$		
	LDA	BP	PW	LDA	BP	PW
AE	158	172	157	251	266	252
FC	160	174	161	258	274	262
PC3	161	175	166	260	277	274*
PC2	164	176	166	268	278	264
PC1	204	213	202	355	360	352
NC	299	303	292	548	548	527

One peculiarity of the spin-polarized PW results should be mentioned. In tables A1 and A2 the two values for PC3 marked by asterisks deviate slightly from a monotonic behaviour from NC towards FC. This deviation was traced back to the strong density variation with the double-hump shape of the PC3 core density (see figure A1(a)), which causes the first and second density derivatives to vary very strongly as well. The first radial density derivatives are plotted in figure A1(b). The PW functional turns out to react very strongly to these strong changes in the density derivatives. Some of this sensitivity stems from the fact that in the usual partial-core correction the spherical Bessel function and the core density are matched continuously only in value and slope, leaving a cusp in the first derivative, which is clearly visible in figure A1 for PC1 and PC3, and a discontinuity in the second derivative and consequently in the effective potential. However, on matching the second derivative continuously as well, we found that the total energies and their differences were improved only marginally. The BP functional, in contrast, does not lead to such a peculiar behaviour. Hence, we attribute the sensitivity, in accordance with previous experience [86–88], to the specific analytic form of the PW functional.

Also, for $[Ar]3d^{6.6}4s^{0.6}4p^{0.8}$ as the atomic reference configuration, we furthermore constructed pseudopotentials for the configurations $[Ar]3d^64s^2$ and $[Ar]3d^74s^1$. All of the results obtained with these different pseudopotentials for the two lowest atomic states agree within 5 mRyd for the spin-polarization energies and within 10 mRyd for the s–d promotion energies. The results for the first reference configuration, which we selected for all of the crystal calculations, are closest to the AE data.

In previous pseudopotential studies of various materials [89, 87] it has been observed that it is often not essential to use ionic pseudopotentials constructed from GC atomic states, and that LDA pseudopotentials are just as accurate for GC calculations for the valence-electron states. Our study with spin-polarized iron atoms and crystals yielded the same behaviour. Therefore, all of the LDA and GGA MBPP results for iron crystals reported in this work were obtained using LDA pseudopotentials (this was found to be justified by means of extensive tests using GC pseudopotentials as well).

Furthermore, like in various studies of other materials, we found again that self-consistency in the GC calculations is not essential for obtaining the properties of iron atoms and crystals considered here. The results from non-self-consistent GC calculations, in which the self-consistent LDA electron densities are used to calculate the GC total energies, turned out to coincide so well with those from self-consistent GC calculations that we felt justified to perform most of the GC pseudopotential calculations using the LDA densities and to

carry out self-consistent GC calculations only to check and confirm selected results. An attractive feature of this procedure is that the GC contributions to the total energies and all derived properties can be nicely separated from the LDA parts to show the influences of the gradient corrections.

In the MBPP crystal calculations, this behaviour is particularly advantageous, because an accurate momentum-space representation of second derivatives of the electron densities, needed for the effective potential in the self-consistency cycles, by Fourier series requires considerably more effort and resources than obtaining the densities themselves and than obtaining the first derivatives, which are only needed for the total-energy functional.

All of our reported GC all-electron results on the other hand, which were intended as references for comparison with the MBPP results, were always obtained self-consistently.

Appendix B. Equations of state

To determine cohesive parameters like the equilibrium volume V_0 of a crystal, the cohesive energy E_0, the bulk modulus B_0 and its pressure derivative B' (e.g. for studies of high-pressure properties of crystals), one commonly calculates total energies as functions of the unit-cell volumes and then fits an analytic model equation of state (EOS) to the $E(V)$ data.

In contrast to basis sets containing a fixed number of functions, like the LMTO basis set and other atom-centred basis sets (LCAO), which yield very smooth $E(V)$ curves, all plane-wave and related basis sets like the mixed basis or the LAPW basis may lead to 'rugged' $E(V)$ curves, because the number of basis functions is determined by a kinetic energy cut-off E_{pw} or E_{apw} (see section 2) and can change discontinuously with the unit-cell volume. Besides keeping the ruggedness sufficiently small by using a sufficiently large value of E_{pw}, one uses the fit of an EOS to the data to eliminate most of the influence of the ruggedness on the cohesive properties.

The simplest scheme for obtaining V_0 and B_0 is a parabola fit, which however is limited to a narrow region around V_0 because it cannot account for the anharmonic shape of $E(V)$.

The 'universal binding curve', an EOS proposed by Rose *et al* for $E(V)$ [64, 65], has been confirmed to be very useful for the description of theoretical $E(V)$ curves for many materials. This EOS contains three free parameters which can be identified with V_0, B_0 and E_0. V_0 marks the minimum position of $E(V)$, B_0 its curvature at V_0 and E_0 the cohesive energy, defined as the energy difference $E_0 = E(V = V_0) - \tilde{E}(V \to \infty)$. To fit these three parameters one needs the total energies of the crystal and, additionally, that of a free atom, $\tilde{E}$, as the zero level. The pressure derivative of the bulk modulus, B', which is often used as a measure of the lattice anharmonicity, is not a free parameter, but is completely fixed by the other three quantities.

A variant of the Rose *et al* EOS is the 'universal equation of state' given by Vinet *et al* [90, 91] for $p(V)$. It has been found reliable for interpolations and extrapolations of experimental high-pressure $V(p)$ data. Here the three independent fit parameters are V_0, B_0 and B'. Integrating the Vinet *et al* EOS for $p(V)$ over V once, one gets an $E(V)$ equation with the analytic form of the Rose *et al* EOS, as expected, but then with the integration constant $\tilde{E}$ as a fourth fit parameter. The four parameters can be determined by fitting to crystalline total energies alone; no atomic total energy is needed. A cohesive energy can be defined as $E_0 = E(V_0) - \tilde{E}$.

As will be shown below, the comparison of the parameters obtained from the Rose *et al* EOS and the Vinet *et al* EOS will allow a critical judgment of the physical significance of the fit parameters—that is, of E_0 and B'.

Two further often-used model EOS are the ones given by Murnaghan [92] and by Birch

[93]. Here again the fit parameters are V_0, B_0 and B'. E_0 is not incorporated in these EOS (like in the case of the parabola), and it is usually determined independently from the difference between the total energy of the crystal at V_0 and that of a free atom.

Table A3. A comparison of cohesive parameters for fcc NM and fcc FM Fe obtained on the basis of four different equations of state (EOS) (for the meaning of the numbers in parentheses, see the main text).

		EOS			
Structure		Rose *et al* [64, 65]	Vinet *et al* [90, 91]	Murnaghan [92]	Birch [93]
fcc NM					
V_0 (Å^3)	MBPP	9.85	9.85	9.85	9.85
	FLAPW	9.70	9.70	9.70	9.70
E_0 (eV)	MBPP	6.33	6.58	—	—
	FLAPW	6.33	6.95	—	—
B_0 (GPa)	MBPP	321	321	318	320
	FLAPW	342	341	336	340
B'	MBPP	(4.5)	4.5	4.5	4.5
	FLAPW	(4.6)	4.5	4.5	4.5
fcc FM					
V_0 (Å^3)	MBPP	11.21	11.36	11.49	11.43
	FLAPW	10.93	10.85	10.99	10.95
E_0 (eV)	MBPP	6.16	2.28	—	—
	FLAPW	6.08	4.71	—	—
B_0 (GPA)	MBPP	208	271	349	295
	FLAPW	209	193	233	215
B'	MBPP	(4.1)	6.8	11.5	7.5
	FLAPW	(4.5)	3.9	6.2	4.8

To illustrate the possible influence of the choice of EOS on the cohesive properties, we choose LDA/LSDA results for fcc NM and fcc FM γ-Fe as an example. The results for the different fit curves are listed in table A3. The results obtained by using the EOS of Rose *et al* for B' are given in parentheses because they were not fitted independently, but are entirely dependent on the other three quantities (see above).

For fcc NM Fe, seven MBPP (six FLAPW) total-energy values surrounding the minimum V_0 approximately symmetrically were included, and the data in table A3 indicate a rather weak dependence on the choice of EOS.

For fcc FM Fe, however, only total-energy values for volumes larger than the expected value of V_0 could be used for the fit because of the magnetic instability at smaller volumes. This asymmetric distribution leads to remarkably large discrepancies between the cohesive properties obtained by using the different EOS. The EOS of Vinet *et al*, that of Murnaghan and that of Birch, which do not fix a free-atom limit, show large differences in the values that they lead to for B_0, B' and E_0. In particular the value obtained for E_0 using the Vinet *et al* EOS, which is strictly defined as the difference between the energy of a non-interacting free atom and that of an atom condensed in a crystal, is not realistic. Furthermore, there is a strong sensitivity of the fit to the number of $E(V)$ data points included (B_0, e.g., changes by several tens of gigapascals on simply including one data point more or less).

In the case of the Rose *et al* EOS, on the other hand, in which the free-atom limit

is assumed to be given by the total energy of a spin-polarized, isolated iron atom in its ground state, the fitting is fairly unambiguous, and the agreement as regards the cohesive parameters obtained by the MBPP and FLAPW methods is more satisfactory.

The example of fcc FM Fe in the LSDA is of course rather extreme and the ambiguity of the results for different EOS is much smaller for cases in which $E(V)$ data on either side of V_0 can be included in the fit. This is the case for fcc FM Fe when using GC total-energy functionals.

For the results for the cohesive properties presented in the main text, we carried out fits to both the Rose *et al* EOS and the Vinet *et al* EOS. In critical cases we assumed a higher reliability of the results obtained with the Rose *et al* EOS.

Appendix C. Cohesive properties of Nb and Pd

In a previous study by our groups [87, 88], the question of a possible improvement of accuracy with respect to that of the LDA achieved by the use of gradient corrections in total-energy calculations for cohesive properties of crystals has been addressed. Meanwhile, a lively discussion has been proceeding in the literature, with emphatic views expressed for and against, but a consensus has been approached as regards the systematics of the changes due to the gradient corrections (i.e. an increase of the equilibrium volume V_0 and a decrease of the bulk modulus B_0 connected with the considerable improvement of a reduction of the theoretical cohesive energy E_0).

Table A4. Equilibrium lattice constants a_0 and bulk moduli B_0 for Nb and for Pd, calculated using the FLAPW method (cf. tables V and VI in reference [87] and table I in [88]).

	Nb		Pd	
	a_0 (Å)	B_0 (GPa)	a_0 (Å)	B_0 (GPa)
4s/4p core				
LDA BH, relativistic	3.31	166	3.88	214
PW, relativistic	3.41	143	4.05	148
PW91, relativistic	3.37	149	3.98	158
4s/4p semicore				
LDA BH, relativistic	3.23	179	3.86	217
PW, relativistic	3.34	149	4.04	140
PW91, relativistic	3.29	168	3.96	162
Experiment [95]	3.30	170	3.89	181

Following our work, we encountered some scepticism as regards the rather strong overcorrection of the equilibrium lattice constants a_0 (or equivalently volumes V_0) of 4d transition metals, in particular of Pd and the surrounding fcc metals, which we determined using both the MBPP and the LMTO–ASA methods. There were speculations that some of the overcorrection might be caused by the pseudopotential approximation on one hand, or might be due to the ASA on the other hand. To test these conjectures, we recalculated the cohesive properties of both of the 4d transition metals Pd and Nb, using the FLAPW method, as implemented in the WIEN93 code [40]. Our results are listed in table A4 and may be compared to the data in tables V and VI of our previous work [87] (see also table

I in reference [88]).

In the FLAPW calculations, the outermost filled 4s and 4p core shells were treated in two different ways. First they were included as true core states, strictly confined to the muffin-tin spheres. The results for this case correspond to the treatment in the LMTO–ASA calculations of [87], and, except for the lattice superposition of frozen atomic partial-core densities in the evaluation of the non-linear xc energy density and potential, also in the MBPP calculations. Second they were treated as band-like semicore states in an energy panel below and separated from the valence-electron energy range.

We find that the CA and PW results clearly confirm our previous results, and the PW91 results are close to the previous BP results, as expected in view of the similar functional forms.

The effect of the semicore treatment on a_0 and B_0 is very weak in the case of Pd, because the 4s and 4p states are energetically far below the valence bands and well localized at the single atomic sites. In the case of Nb, however, there is a rather soft outer core, leading to a considerable contraction of a_0 and increase of B_0 in the LDA. Whereas the core result for a_0 matches almost perfectly the quoted experimental value, the semicore result for a_0 is noticeably too small. The application of the gradient corrections PW and PW91 increases the a_0-values and leads to an overestimation in the core case but to a good coincidence with experiment in the semicore case.

However, comparing Nb and Pd, we hesitate to conclude from the results for Nb alone that the semicore treatment and the use of PW91 yields the ultimate result and the best agreement with experiment, because for Pd, PW91 yields similar overcorrections for the core case and the semicore case. The soft 4s–4p cores in the transition metals with few 4d electrons are very delicate and we suspect that they may need an even more accurate treatment than that via a semicore energy panel in the FLAPW method—for instance, perhaps via including additional local orbitals in the LAPW basis [94], in order to achieve basis-set-independent accuracy within the LDA or with gradient corrections.

References

[1] Hohenberg P and Kohn W 1964 *Phys. Rev.* **136** B864
[2] Kohn W and Sham L J 1965 *Phys. Rev.* **140** A1133
[3] Schlapbach L (ed) 1988 *Hydrogen in Intermetallic Compounds I* (Berlin: Springer)
[4] Fukai Y 1993 *The Metal–Hydrogen System* (Berlin: Springer)
[5] Ho K-M, Tao H-J and Zhu X-Y 1984 *Phys. Rev. Lett.* **53** 1586
[6] Tao H-J, Ho K-M and Zhu X-Y 1986 *Phys. Rev.* B **34** 8394
[7] Elsässer C, Ho K M, Chan C T and Fähnle M 1991 *Phys. Rev.* B **44** 10 377
[8] Elsässer C, Ho K M, Chan C T and Fähnle M 1992 *J. Phys.: Condens. Matter* **4** 5207
[9] Elsässer C 1994 Ab-initio-Elektronentheorie für Übergangsmetall-Wasserstoff-Verbindungen *Habilitationsschrift* Universität Stuttgart
[10] Badding J V, Hemley R J and Mao H K 1991 *Science* **253** 421
[11] Louie S G, Ho K-M and Cohen M L 1979 *Phys. Rev.* B **19** 1774
[12] Fu C-L and Ho K-M 1983 *Phys. Rev.* B **28** 5480
[13] Elsässer C, Takeuchi N, Ho K M, Chan C T, Braun P and Fähnle M 1990 *J. Phys.: Condens. Matter* **2** 4371
[14] Ho K M, Elsässer C, Chan C T and Fähnle M 1992 *J. Phys.: Condens. Matter* **4** 5189
[15] von Barth U and Hedin L 1972 *J. Phys. C: Solid State Phys.* **5** 1629
[16] Perdew J P 1986 *Phys. Rev.* B **33** 8822
[17] Perdew J P 1986 *Phys. Rev.* B **34** 7406 (erratum to [16])
[18] Perdew J P and Wang Y 1986 *Phys. Rev.* B **33** 8800
[19] Becke A D 1988 *Phys. Rev.* A **38** 3098
[20] Perdew J P 1991 *Electronic Structure of Solids 91* ed P Ziesche and H Eschrig (Berlin: Akademie)
[21] Greenside H S and Schlüter M A 1983 *Phys. Rev.* B **27** 3111

[22] Zhu J, Wang X W and Louie S G 1992 *Phys. Rev.* B **45** 8887
[23] Sasaki T, Rappe A M and Louie S G 1995 *Phys. Rev.* B **52** 12 760
[24] Cho J-H and Scheffler M 1996 *Phys. Rev.* B **53** 10 685
[25] Kishi T and Itoh S 1995 *J. Phys.: Condens. Matter* **7** 6197
[26] Elsässer C, Zhu J, Louie S G, Meyer B, Fähnle M and Chan C T 1998 *J. Phys.: Condens. Matter* **10** 5113
[27] Elsässer C, Krimmel H, Fähnle M, Louie S G and Chan C T 1998 *J. Phys.: Condens. Matter* **10** 5131
[28] Krimmel H, Schimmele L, Elsässer C and Fähnle M 1994 *J. Phys.: Condens. Matter* **6** 7705
[29] Pickett W E 1989 *Comput. Phys. Rep.* **9** 115
[30] Payne M C, Teter M P, Allen D C, Arias T A and Joannopoulos J D 1992 *Rev. Mod. Phys.* **64** 1045
[31] Ihm J, Zunger A and Cohen M L 1979 *J. Phys. C: Solid State Phys.* **12** 4409
[32] Ihm J, Zunger A and Cohen M L 1980 *J. Phys. C: Solid State Phys.* **13** 3095 (erratum to [31])
[33] Chadi D J and Cohen M L 1973 *Phys. Rev.* B **8** 5747
[34] Moreno J and Soler J M 1992 *Phys. Rev.* B **45** 13 891
[35] Elsässer C, Fähnle M, Chan C T and Ho K M 1994 *Phys. Rev.* B **49** 13 975
[36] Vanderbilt D 1985 *Phys. Rev.* B **32** 8412
[37] Louie S G, Froyen S and Cohen M L 1982 *Phys. Rev.* B **26** 1738
[38] Andersen O K 1975 *Phys. Rev.* B **12** 3060
[39] Koelling D D and Arbman G O 1975 *J. Phys. F: Met. Phys.* **5** 2041
[40] Blaha P, Schwarz K and Augustyn R 1993 *WIEN93* Technical University of Vienna
This is an improved and updated Unix version of the original copyrighted WIEN code, which was published in
Blaha P, Schwarz K, Sorantin P and Trickey S B 1990 *Comput. Phys. Commun.* **59** 399
[41] Andersen O K and Jepsen O 1984 *Phys. Rev. Lett.* **53** 2571
[42] Monkhorst H J and Pack J D 1976 *Phys. Rev.* B **13** 5188
[43] Blöchl P E, Jepsen O and Andersen O K 1994 *Phys. Rev.* B **49** 16 223
[44] Perdew J P and Zunger A 1981 *Phys. Rev.* B **23** 5048
[45] Ceperley D M and Alder B J 1980 *Phys. Rev. Lett.* **45** 566
[46] Hedin L and Lundqvist B I 1971 *J. Phys. C: Solid State Phys.* **4** 2064
[47] Moruzzi V L, Janak J F and Williams A R 1978 *Calculated Electronic Properties of Metals* (New York: Pergamon)
[48] Perdew J P, Chevary J A, Vosko S H, Jackson K A, Pederson M R, Singh D J and Fiolhais C 1992 *Phys. Rev.* B **46** 6671
[49] Perdew J P, Chevary J A, Vosko S H, Jackson K A, Pederson M R, Singh D J and Fiolhais C 1993 *Phys. Rev.* B **48** 4978 (erratum to [48])
[50] Terakura K, Oguchi T, Williams A R and Kübler J 1984 *Phys. Rev.* B **30** 4734
[51] Dufek P, Blaha P, Sliwko V and Schwarz K 1994 *Phys. Rev.* B **49** 10 170
[52] Jansen H J F, Hathaway K B and Freeman A J 1984 *Phys. Rev.* B **30** 6177
[53] Wang C S, Klein B M and Krakauer H 1985 *Phys. Rev. Lett.* **54** 1852
[54] Hathaway K B, Jansen H J F and Freeman A J 1985 *Phys. Rev.* B **31** 7603
[55] Jansen H J F and Peng S S 1988 *Phys. Rev.* B **37** 2689
[56] Bagno P, Jepsen O and Gunnarsson O 1989 *Phys. Rev.* B **40** 1997
[57] Barbiellini B, Moroni E G and Jarlborg T 1990 *J. Phys.: Condens. Matter* **2** 7597
[58] Singh D J, Pickett W E and Krakauer H 1991 *Phys. Rev.* B **43** 11 628
[59] Moruzzi V L, Marcus P M, Schwarz K and Mohn P 1986 *Phys. Rev.* B **34** 1784
[60] Moruzzi V L, Marcus P M and Kübler J 1989 *Phys. Rev.* B **39** 6957
[61] Kübler J 1989 *Solid State Commun.* **72** 631
[62] Uhl M, Sandratskii L M and Kübler J 1994 *Phys. Rev.* B **50** 291
[63] Mryasov O N, Gubanov V A and Liechtenstein A I 1992 *Phys. Rev.* B **45** 12 330
[64] Rose J H, Ferrante J and Smith J R 1981 *Phys. Rev. Lett.* **47** 675
[65] Rose J H, Smith J R, Guinea F and Ferrante J 1984 *Phys. Rev.* B **29** 2963
[66] Amador C, Lambrecht W R L and Segall B 1992 *Phys. Rev.* B **46** 1870
[67] Körling M and Häglund J 1992 *Phys. Rev.* B **45** 13 293
[68] Stixrude L, Cohen R E and Singh D J 1994 *Phys. Rev.* B **50** 6442
[69] Elsässer C, Zhu J, Louie S G, Ho K M, Chan C T and Fähnle M 1992 *Bull. Am. Phys. Soc.* **37** 198
[70] *Landolt–Börnstein New Series* 1987 Group III, vol 19a (Berlin: Springer)
[71] Alefeld G and Völkl J (ed) 1978 *Hydrogen in Metals II* (Berlin: Springer)
[72] Leung T C, Chan C T and Harmon B N 1991 *Phys. Rev.* B **44** 2923
[73] MacLaren J M, Clougherty D P and Albers R C 1990 *Phys. Rev.* B **42** 3205

[74] Papaconstantopoulos D A 1991 *Europhys. Lett.* **15** 621
[75] Stoner E C 1938 *Proc. R. Soc.* A **165** 372
[76] Wohlfarth E P 1953 *Rev. Mod. Phys.* **25** 211
[77] Vosko S H and Perdew J P 1975 *Can. J. Phys.* **53** 1325
[78] Singh D J and Papaconstantopoulos D A 1994 *Phys. Rev.* B **49** 12 801
[79] Philipp S, Leiberich R, Schmidt P C and Weiss A 1993 *Intermetallics* **1** 227
[80] Seeger A and Schimmele L 1992 *Perspectives of Meson Science* ed T Yamazaki, K Nakai and K Nagamine (Amsterdam: Elsevier) p 293
[81] Staiger W 1990 *Doktorarbeit* Universität Stuttgart
[82] Akai M, Akai H and Kanamori J 1983 *J. Magn. Magn. Mater.* **31–34** 551
[83] Kanamori J, Akai H and Akai M 1984 *Hyperfine Interact.* **17–19** 287
[84] Ellis D E and Lindgren B 1984 *Hyperfine Interact.* **17–19** 279
[85] Fähnle M, Hummler K, Liebs M and Beuerle T 1993 *Appl. Phys.* A **57** 67
[86] Ortiz G and Ballone P 1991 *Phys. Rev.* B **43** 6376
[87] García A, Elsässer C, Zhu J, Louie S G and Cohen M L 1992 *Phys. Rev.* B **46** 9829
[88] García A, Elsässer C, Zhu J, Louie S G and Cohen M L 1993 *Phys. Rev.* B **47** 4150 (erratum to [87])
[89] Kong X J, Chan C T, Ho K M and Ye Y Y 1990 *Phys. Rev.* B **42** 9357
[90] Vinet P, Ferrante J, Smith J R and Rose J H 1986 *J. Phys. C: Solid State Phys.* **19** L467
[91] Vinet P, Rose J H, Ferrante J and Smith J R 1989 *J. Phys.: Condens. Matter* **1** 1941
[92] Murnaghan F D 1951 *Finite Deformation of an Elastic Solid* (New York: Wiley)
[93] Birch F 1952 *J. Geophys. Res.* **457** 227
[94] Singh D 1991 *Phys. Rev.* B **43** 6388
[95] Kittel C 1986 *Introduction to Solid State Physics* (New York: Wiley)
[96] Zarestky J and Stassis C 1987 *Phys. Rev.* B **35** 4500